The Astrophysical Journal, 976:87 (24pp), 2024 November 20 https://doi.org/10.3847/1538-4357/ad7c4e

Accurate, Precise, and Physically Self-consistent Ages and Metallicities for 400,000 Solar Neighborhood Subgiant Branch Stars

David M. Nataf[1,2], Kevin C. Schlaufman[2], Henrique Reggiani[3,4], and Isabel Hahn[4,5]
[1] Department of Physics & Astronomy, University of Iowa, Iowa City, IA 52242, USA; david-nataf@uiowa.edu
[2] William H. Miller III Department of Physics & Astronomy, Johns Hopkins University, 3400 N Charles St. Baltimore, MD 21218, USA
[3] Gemini Observatory/NSF's NOIRLab, Casilla 603, La Serena, Chile
[4] The Observatories of the Carnegie Institution for Science, 813 Santa Barbara St. Pasadena, CA 91101, USA
[5] Department of Physics and Astronomy, Pomona College, Claremont, CA 91711, USA
Received 2023 December 16; revised 2024 July 16; accepted 2024 July 17; published 2024 November 14

Abstract

Age is the most difficult fundamental stellar parameter to infer for isolated stars. While isochrone-based ages are in general imprecise for both main-sequence dwarfs and red giants, precise isochrone-based ages can be obtained for stars on the subgiant branch transitioning from core to shell hydrogen burning. We synthesize Gaia Data Release 3–based distance inferences, multiwavelength photometry from the ultraviolet to the mid-infrared, and three-dimensional extinction maps to construct a sample of 289,759 solar-metallicity stars amenable to accurate, precise, and physically self-consistent age inferences. Using subgiants in the solar-metallicity open clusters NGC 2682 (i.e., M67) and NGC 188, we show that our approach yields accurate and physically self-consistent ages and metallicities with median statistical precisions of 8% and 0.06 dex, respectively. The inclusion of systematic uncertainties resulting from nonsingle or variable stars results in age and metallicity precisions of 9% and 0.12 dex, respectively. We supplement this solar-metallicity sample with an additional 112,062 metal-poor subgiants, including over 3000 stars with $[\mathrm{Fe/H}] \lesssim -1.50$, 7% age precisions, and apparent Gaia G-band magnitudes $G < 14$. We further demonstrate that our inferred metallicities agree with those produced by multiplexed spectroscopic surveys. As an example of the scientific potential of this catalog, we show that the solar neighborhood star formation history has three components at $([\mathrm{Fe/H}], \tau/\mathrm{Gyr}) \approx (+0.0, 4)$, $(+0.2, 7)$, and a roughly linear sequence in age–metallicity space beginning at $([\mathrm{Fe/H}], \tau/\mathrm{Gyr}) \approx (+0.2, 7)$ and extending to $(-0.5, 13)$. Our analyses indicate that the solar neighborhood includes stars on disk-like orbits even at the oldest ages and lowest metallicities accessible by our samples.

Unified Astronomy Thesaurus concepts: Stellar ages (1581); Solar neighborhood (1509); Galactic archaeology (2178); Milky Way disk (1050); Milky Way dynamics (1051); Milky Way formation (1053); Milky Way stellar halo (1060); Population II stars (1284); Stellar astronomy (1583); Subgiant stars (1646)

Materials only available in the online version of record: machine-readable table

1. Introduction

Inferring the ages of isolated field stars, and by extension, the star formation history of the solar neighborhood, remains among the most challenging and most fundamental problems of Galactic astronomy (e.g., B. A. Twarog 1980; D. R. Soderblom 2010; L. Casagrande et al. 2016). Several approaches are currently being both widely used and developed, including asteroseismic age estimates (S. Sharma et al. 2019; A. Miglio et al. 2021), probabilistically weighted isochrone-based ages (F. Pont & L. Eyer 2004; B. R. Jørgensen & L. Lindegren 2005; D. K. Feuillet et al. 2018; C. A. L. Bailer-Jones et al. 2021), rotation-based ages (S. A. Barnes 2007; J. Chanamé & I. Ramírez 2012), and radioactivity-based ages (C. Sneden et al. 1996; J. J. Cowan et al. 2002). Each of these comes with their own specific strengths, successes, selection effects, and limitations.

In this investigation we focus on a specific class of isochrone-based ages—that of stars along the subgiant branch. These are the stars which are transitioning from core to shell hydrogen burning. The luminosities of subgiants are strong functions of their core masses (M. Salaris & S. Cassisi 2005; R. Kippenhahn et al. 2013). Since core mass scales with stellar mass, and main-sequence lifetime scales with stellar mass, luminosity on the subgiant branch is also a function of age. It can be estimated quantitatively (see Figure 1) that the absolute magnitude M of a subgiant star scales with age at a level approximating:

$$M_1 - M_2 \approx \ln(\tau_2/\tau_1), \quad (1)$$

and thus a 1% measurement in the absolute magnitude of a subgiant star approximately corresponds to a 1% measurement in its relative, model-dependent age, with the exact dependence being a function of location on the subgiant branch, age, and metallicity. It follows that if parallax measurements with 1% precision are available, the theoretical lower bound on the derived ages of subgiants is approximately 2%. Among the other advantages of subgiants are (i) they are bright, and thus detailed elemental abundance measurements can be obtained to large distances, and (ii) they are numerous for stellar populations older than $\tau \approx 1$ Gyr, enabling study of intermediate and old stellar populations with a quantifiable bias.

In this investigation we neglect to account for possible variations in the initial helium abundances of stars, and of their initial rotation, which can affect the relationship between ages

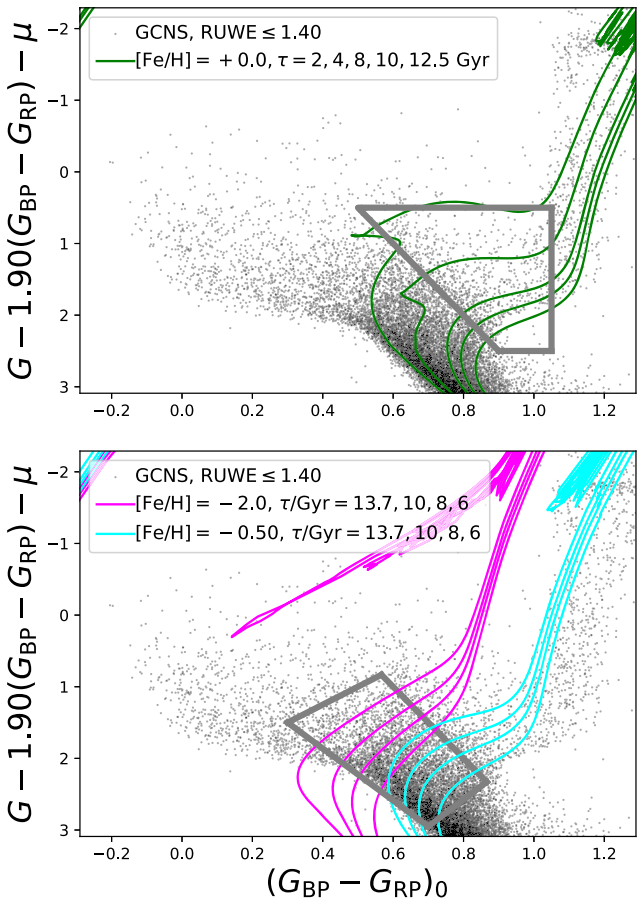

Figure 1. We show our color–magnitude selection function (thick gray lines) overplotted on the Gaia Catalog of Nearby Stars (small black points) with MIST isochrones for the main sample (top) and the metal-poor annex (bottom).

and luminosity on the subgiant branch (A. Marín-Franch et al. 2010; D. M. Nataf et al. 2012; A. A. R. Valcarce et al. 2012; G. Valle et al. 2015). A recent investigation of subgiants with Kepler asteroseismology has found that age inferences of subgiant stars are much more sensitive to uncertainties in the assumed metallicities than in either the initial helium abundance or the mixing length assumed by stellar models (T. Li et al. 2020). It is also the case that prior investigations have shown that scaled solar helium abundances are a good fit to the data for most solar neighborhood stars (L. Casagrande et al. 2007). Unidentified blends and binaries are undoubtedly a source of systematic error, which we explore later in this work.

A recent study of the local stellar age distribution using ∼250,000 subgiant stars is that of M. Xiang & H.-W. Rix (2022). Their methodology differs from ours in several respects, most significantly that they constrain their stellar metallicities using spectroscopically derived measurements from LAMOST (L.-C. Deng et al. 2012; G. Zhao et al. 2012; M. Xiang et al. 2019), whereas we use photometric measurements across the available wavelength regime, including ultraviolet measurements, which are the most sensitive to metallicity. We also note that in principle one can fit for stellar parameters using the spectra themselves, as done by R. Schönrich & M. Bergemann (2014), rather than to the stellar parameters derived from the spectra.

The advantage of the approach that we develop and employ here is the potential for a large, all-sky sample of subgiants with exquisitely measured stellar parameters. Much of our ultraviolet data comes from the Galaxy Evolution Explorer (GALEX; P. Morrissey et al. 2007), which will be augmented in the future with missions such as ULTRASAT (Y. Shvartzvald et al. 2024) and UVEX (S. R. Kulkarni et al. 2021). Owing to the significant leverage of GALEX photometry in inferring stellar atmospheric parameters such as metallicity (S. G. Sichevskij et al. 2014; S. Mohammed et al. 2019; X. Lu et al. 2024), in combination with all-sky astrometric, photometric, variability, and spectroscopic surveys such as Gaia (Gaia Collaboration et al. 2016), as well as all-sky extinction maps (L. Capitanio et al. 2017; G. M. Green et al. 2019; J. L. Vergely et al. 2022), we should eventually be able to measure the precise stellar parameters (including age) for up to $\mathcal{O}(10^7)$ subgiants. That is a regime where we can expect to be able to resolve individual star formation events, and thus bring unprecedented resolution to the story of the Milky Way's formation and assembly.

In this investigation, we develop the method of astrophotometric age and composition inferences of subgiant stars, with the aims of producing a catalog for further study, identifying and quantifying the strengths and limitations of this method, and charting a path for robust future study. The structure of this paper is as follows. In Section 2, we describe how we build our sample. In Section 3, we test our methodology in seven specific ways. Our results are presented in Section 4. We conclude in Section 5.

2. Sample Selection

We select our subgiant sample using a combination of Gaia Data Release 3 (DR3) magnitudes, distances from C. A. L. Bailer-Jones et al. (2021), and reddening estimates as discussed in Section 2.3 and in our Appendix. The magnitudes that we use for our sample selection are the nearly extinction-independent absolute Wesenheit magnitudes:

$$W_G = G - 1.90(G_{\rm BP} - G_{\rm RP}) - 5\log(d/pc) + 5, \quad (2)$$

and colors that we use are:

$$(G_{\rm BP} - G_{\rm RP})_0 = (G_{\rm BP} - G_{\rm RP}) - 0.424A_V. \quad (3)$$

The color and magnitude criteria for our main sample (top panel of Figure 1) are:

1. $W_G \leqslant 2.50$;
2. $W_G \geqslant +0.50$;
3. $W_G \leqslant 2.50 + 5((G_{\rm BP} - G_{\rm RP})_0 - 0.90)$;
4. $(G_{\rm BP} - G_{\rm RP})_0 \leqslant 1.05$; and
5. at least one measurement of GALEX near-ultraviolet (NUV), Skymapper u ($u_{\rm SM}$), or Sloan Digital Sky Survey (SDSS) u ($u_{\rm SDSS}$).

This subgiant sample inevitably includes some stars on the turnoff and the base of the red giant branch, as the location of these phases of stellar evolution on the color–magnitude diagram is a sensitive function of age and metallicity. The primary sample defined above is most efficient at targeting stars with $-0.50 \lesssim$ [Fe/H] $\lesssim +0.50$. Subgiant stars of lower metallicity appear at the same location in the Gaia DR3 color–magnitude diagram as the vastly more numerous more metal-rich turnoff stars, and thus finding them would otherwise be akin to searching for a needle in a haystack, but we can delineate them by making use of metallicity-sensitive ultraviolet photometry. We select the metal-poor annex (bottom panel of Figure 1) using the following criteria:

1. $W_G > 2.50 + 5((G_{BP} - G_{RP})_0 - 0.90)$;
2. $W_G \geqslant 1.5 - 2.5((G_{BP} - G_{RP})_0 - 0.30)$;
3. $W_G \leqslant 1.5 + 3.625((G_{BP} - G_{RP})_0 - 0.30)$;
4. $W_G \leqslant 2.95 - 3.75((G_{BP} - G_{RP})_0 - 0.70)$;
5. at least one measurement of GALEX NUV, Skymapper u, or SDSS u; and
6. each available ultraviolet measurement satisfies the relevant equation of: $(\mathrm{NUV} - G) \leqslant -0.65 + 13/2(G_{BP} - G_{RP})$, $(u_{SM} - G) \leqslant 0.19 + 11/6(G_{BP} - G_{RP})$, and $(u_{SDSS} - G) \leqslant 0.11 + 11/6(G_{BP} - G_{RP})$.

We also require the following photometric, variability, reliability, and reddening criteria, for both samples:

1. measurements in all three of of J, H, K_s from the Two Micron All-Sky Survey (2MASS);
2. measurements in both of W_1 and W_2 from the Wide-field Infrared Survey Explorer (WISE);
3. from Gaia DR3, `parallax_over_error` $\geqslant 50$;
4. from Gaia DR3, `duplicated_source = "FALSE"`;
5. from Gaia DR3, `phot_proc_mode = 0`;
6. from Gaia DR3, `phot_variable_flag != "VARIABLE"`;
7. from Gaia DR3, `non_single_star = 0`;
8. from Gaia DR3, `ruwe` $\leqslant$ `1.4`;
9. from Gaia DR3, `ipd_gof_harmonic_amplitude` $\leqslant$ `0.10`;
10. from Gaia DR3, `astrometric_params_solved = 31` ;
11. no match in the ASAS-SN catalog of variable stars (B. J. Shappee et al. 2014; T. Jayasinghe et al. 2021; C. T. Christy et al. 2023); and
12. $A_V \leqslant 0.50$.

The selection function (in Gaia photometry) is shown in Figure 1, where we also show the color–magnitude diagram of the Gaia Catalog of Nearby Stars (Gaia Collaboration et al. 2021) and [Fe/H] = −2.00, −0.50, and +0.00 isochrones from MIST (B. Paxton et al. 2011, 2013, 2015; J. Choi et al. 2016; A. Dotter 2016) for comparison.

The selection function described in this section was formed from a combination of guidelines in the input data, as well as arbitrary delineations meant to optimize the trade-off between selecting more subgiants and selecting fewer turnoff and red giant stars.

2.1. Additional Photometric Criteria

Ideally, crossmatching point sources between different photometric surveys would be conducted using purely astrometric criteria. In practice, that leads to spurious crossmatches due to factors such as the varying astrometric precision and accuracy between the different surveys, the varying size of the point-spread function (PSF) and thus sensitivity to blends, that the sensitivity to blends will itself be wavelength and thus bandpass dependent, and the different saturation limits and photometric depths of each survey.

We implement the ad hoc requirement that in the posterior calculation for each star, the predicted apparent magnitudes in GALEX NUV, 2MASS J, WISE W_2, SDSS ug, Skymapper uvg, and Pan-STARRS gy differ by no more than 3σ with the observed magnitudes. In each case, the photometric errors given by the catalogs are inflated by 0.01 mag in quadrature, and the total number of stars flagged as having less certain photometric matches is 9609 in the primary sample. We find that the number of flagged stars is typically 5× what one would expect from purely statistical errors. Upon inspection, we find that most of the matches are due to large offsets between the apparent and predicted magnitudes—plausibly mismatches or blends.

In the example of NUV, our criteria flags 2936 stars from our sample of 229,156 stars with NUV matches, which is approximately 5× greater than the expectation from pure statistical expectations. For those flagged stars, the mean and 1σ astrometric offset between Gaia DR3 and GALEX is $0.''7 \pm 0.''5$, whereas for the sample as a whole the separation is distributed as $0.''5 \pm 0.''4$. The larger mean and scatter in the astrometric separations are consistent with the inclusion of more spurious matches.

2.2. Additional Variability Criteria

We use two additional variability criteria to flag stars as less reliable probes of single-star stellar evolution. We still compute the posteriors for these parameters of these stars, and still report them in our data tables, but we do not include the results in our analysis.

The first additional criterion is based on the Gaia G-band photometric variability of the star. For each star in our main sample, we compute the photometric variability σ_G as follows:

$$\sigma_G = (\mathrm{phot\_g\_mean\_flux\_error})(\sqrt{phot\_g\_n\_obs}), \quad (4)$$

and we then compute the percentile for σ_G for each star at the apparent magnitude of that star, in our primary sample. We use that percentile as an indicator of photometric variability, though it is certainly a coarse proxy, as the number of measurements is sparse for many of the stars.

We find that that requiring that the percentile of σ_G be below the 95th yields a reasonable metric for removing variables. For stars with σ_G below the 95th percentile, approximately 4% have a derived [Fe/H] less than or equal to −0.50, whereas the fraction rises to 9% for stars with a σ_G above the 95th percentile. In all cases discussed here, we also remove stars flagged as having less reliable photometric matches. A reasonable explanation for this trend, whereby more photometrically variables are inferred to more frequently have a low metallicity, is that rapidly rotating stars have bluer spectra, with the effect becoming larger at smaller wavelengths, mimicking metal-poor atmospheres (Luca Casagrande, private communication, using models discussed in L. Casagrande & D. A. VandenBerg 2014).

The second criterion makes use of the work of Q. Chance et al. (2022), who studied the inferred measurement errors in the radial velocity measurements reported by Gaia. They showed that these are associated with spectroscopic binaries, which have the effect of broadening the spectra that are binned from different measurements taken at different times. In the context of our study, unresolved spectroscopic binaries would shift the colors from those expected from single-stellar evolution, and also include a population of past or present mass-transfer binaries, such as blue stragglers.

The criterion suggested by Q. Chance et al. (2022) is one where the p-value to the radial velocity noise satisfies $p \leqslant 0.001$, where they stress that the p-value in their analysis represents the likelihood that the source's radial velocity noise is indeed anomalously high compared to stars of similar color and magnitude.

Of the 289,756 stars in our primary subgiant sample, 266,443 are not flagged as either having less reliable photometric crossmatches or having photometric variability above the 95th percentile. Of those, Q. Chance et al. (2022) reported p-values for 118,636 Gaia sources, for which 23,898, or 20%, have p-values $\leqslant 0.001$ and thus are likely spectroscopic binaries. These 23,898 stars are flagged in our data tables and removed from the subsequent analysis discussed in this paper. Our total sample used for analysis in this paper are those stars with variability below the 95th percentile, with no photometry flagged as spurious, and for which Q. Chance et al. (2022) either reported no p-value or one greater than 0.001; this sample numbers 242,545 point sources.

2.3. Selection of Astrometric, Photometric, and Extinction Data

Our analysis incorporates the following data as input.

1. Parallaxes (π) measurements and associated uncertainties from Gaia Early DR3 (Gaia Collaboration et al. 2023), as well as estimates on the distances derived therefrom (C. A. L. Bailer-Jones et al. 2021) and parallax zero-point corrections from L. Lindegren et al. (2021). $G_{\rm BP}$, G, and $G_{\rm RP}$ magnitudes and associated uncertainties are taken from Gaia Data Release 2 (DR2; Gaia Collaboration et al. 2018b).
2. Far-ultraviolet (FUV) and NUV magnitudes and associated uncertainties are taken from the revised catalog of GALEX ultraviolet sources (L. Bianchi et al. 2017).
3. u, g, r, i, and z magnitudes and associated uncertainties are taken from the SDSS (R. Ahumada et al. 2020).
4. u, v, g, r, i, and z magnitudes and associated uncertainties are taken from DR2 of the SkyMapper Southern Sky Survey (C. A. Onken et al. 2019).
5. g, r, i, z, and y photometry are taken from the Pan-STARRS1 (PS1) catalog (H. A. Flewelling et al. 2020).
6. J, H, and $K_{\rm s}$ magnitudes and associated uncertainties are taken from the 2MASS Point Source Catalog (M. F. Skrutskie et al. 2006).
7. $W1$ and $W2$ magnitudes and associated uncertainties are taken from the WISE AllWISE Source Catalog (E. L. Wright et al. 2010; A. Mainzer et al. 2011; R. M. Cutri et al. 2021).
8. We use the extinction maps of G. M. Green et al. (2019), setting $A_V = 3.04E(g-r)$, for those sight lines for which the quality flags for "converged" and "reliable_dist" are both equal to "TRUE". For the majority of the remaining sight lines, we use the extinction estimates of R. Lallement et al. (2022) and J. L. Vergely et al. (2022), specifically from the version 2 medium-resolution 6 kpc × 6 kpc × 0.8 kpc grid "explore_cube_density_values_025pc_v2.fits." In order to make these consistent to first order with the extinction maps of G. M. Green et al. (2019), we apply the following corrections: (i) $A_V = A_{5500}/0.978$, (ii) $A_V|_{A_V \geqslant 0.15} = A_V|_{A_V \geqslant 0.15} + 0.05$, and (iii) $A_V|_{A_V \leqslant 0.15} = (4/3) \times A_V|_{A_V \leqslant 0.15}$, with the errors subsequently inflated to $\sigma_{A_V} = 0.31 \times A_V$. Finally, for stars for which neither extinction map provides measurements, we use the Schlegel, Finkbeiner, and Davis (SFD) maps (D. J. Schlegel et al. 1998), with the value of $A_V = 2.742E(B-V)$ suggested by the recalibration of E. F. Schlafly & D. P. Finkbeiner (2011).

For each of these parameters, we require that the data satisfy quality flags which we describe in the Appendix. We also inflate all photometric errors by the arbitrary value of 0.01 mag in quadrature.

2.4. Contributions to the Likelihood Function

We construct our likelihood function with the aim of incorporating as many reliable measurements as possible, but to do so without redundancy, as many of the measurements probe nearly identical wavelength regimes. We thus use the following inclusion criteria for our likelihood function.

1. We require at least one measurement of {NUV, $u_{\rm SM}$, $u_{\rm SDSS}$}.
2. If measurements of both of {$u_{\rm SM}$, $u_{\rm SDSS}$} are available, we use that of $u_{\rm SDSS}$.
3. If a measurement of $v_{\rm SM}$ is available, we use it.
4. We require a measurement of G, and we use it.
5. We use whichever has the most available measurements of {$G_{\rm BP}$,$G_{\rm RP}$}, {$g_{\rm SM}$, $r_{\rm SM}$, $i_{\rm SM}$, $z_{\rm SM}$}, {$g_{\rm SSDSS}$, $r_{\rm SDSS}$, $i_{\rm SDSS}$, $z_{\rm SDSS}$}, and {$g_{\rm PS}$, $r_{\rm PS}$, $i_{\rm PS}$, $z_{\rm PS}$}, where "PS" stands for Pan-STARRS. If the number of available measurements are equal, we prioritize those of Pan-STARRS, then SDSS, then Skymapper, then Gaia.
6. If a measurement of $y_{\rm PS}$ is available, we use it.
7. We require and use measurements for each of 2MASS {J, H, K_s} and WISE {W_1, W_2}.
8. If the extinction measurement is from either the PS1 maps, or the J. L. Vergely et al. (2022) or R. Lallement et al. (2022) maps, we use it with the associated measurement errors, where the latter is as described in Section 2.3. If the extinction measurement is from the SFD maps, it does not contribute to the likelihood.
9. We use the parallaxes and associated uncertainties from the Gaia DR3 catalog, with the zero-point corrections from L. Lindegren et al. (2021).

We keep track of all photometric measurements and model predictions thereof, even those not contributing to the likelihood functions, for purposes of subsequent heuristic comparisons.

2.5. Contributions to the Priors

We use the following priors for the exploration of the parameter space for each star.

1. A flat prior in metallicity, over the interval $-2.0 \leqslant [{\rm Fe/H}] \leqslant +0.50$.
2. A flat prior in age in the interval $1 \leqslant \tau/{\rm Gyr} \leqslant 13.721$.
3. A Chabrier prior in the mass of the star, restricted to the range $0.70 \leqslant m/m_{\odot} \leqslant 2.0$.
4. A flat prior in extinction over the interval $A_V - 3\delta_{A_V} \leqslant A_V \leqslant A_V + 3\delta_{A_V}$, where $\delta_{A_V} = \sqrt{\sigma_{A_V}^2 + 0.01^2}$. Here, σ_{A_V} is either the value given for the uncertainty in extinction from the PS1 or R. Lallement et al. (2022) or J. L. Vergely et al. (2022) maps, if those are used, or equal to 10% of the extinction if we use the value from the SFD maps. If the value of $A_V - 3\delta_{A_V}$ is negative, the lower bound on the extinction is set to 0.
5. A prior in distance that is proportional to the square of the distance (and thus uniform in volume), but restricted to the range $1/(\pi + 3\sigma_{\pi}) \leqslant d \leqslant 1/(\pi - 3\sigma_{\pi})$.

3. Methodology and Validation Thereof

We compute the posteriors for the parameters of each star in our sample using the `isochrones` package (T. D. Morton 2015),[6] which uses the PyMultinest implementation (J. Buchner et al. 2014) of `MultiNest` (F. Feroz & M. P. Hobson 2008; F. Feroz et al. 2009, 2019) to compare astrometric, photometric, and spectroscopic observations of stars to predictions from MIST isochrones. The isochrones package has now been widely used to estimate stellar parameters (e.g., B. T. Montet et al. 2015; D. Huber et al. 2016; S. M. Mills et al. 2016; H. Reggiani et al. 2022b) as has MultiNest in other contexts such as microlensing (e.g., R. Poleski et al. 2017), where it has been demonstrated to be effective and efficient in the exploration of degenerate likelihood spaces as well as those with multiple modes.

The isochrones package fully explores the MIST isochrones within the bounds of the priors, by varying the distance, age, initial mass, [Fe/H], and A_V at which the isochrones are evaluated. That is done by interpolating in the variable equivalent evolutionary point (EEP), and using the bolometric correction tables from MIST.[7]

We use seven different methods to validate and investigate our methodology, which we discuss below.

3.1. Validation of the Diagnostic Potential of Photometric Measurements Along the Subgiant Branch

In Figure 2, we plot the scatters of various photometric color measurements of stars in the GALAH survey (G. M. De Silva et al. 2015; S. Buder et al. 2021). These are selected to be on or near the subgiant branch ($3.25 \leqslant \log g \leqslant 4.25$), to have relatively reliable spectroscopic metallicity determinations ($-2.00 \leqslant$ [Fe/H] $\leqslant +0.50$, $\sigma_{\rm [Fe/H]} \leqslant 0.20$), and to have low extinctions ($A_{Ks} \leqslant 0.03$). We compare these to the predictions from the MIST isochrones with ([Fe/H], τ/Gyr) = (−2.0, 10), (−1, 10), (−0.50, 4), and (+0.25, 4) with $3.25 \leqslant \log g \leqslant 4.25$.

We draw several conclusions from this comparison. The first is that measurements in NUV, u, and v are particularly sensitive to metallicity. The second is that the black arrow ($\delta A_V = 0.50$ mag) is usually nearly parallel and approximately 30% longer than the gray arrow ($\delta T_{\rm eff} = 500$ K), and thus the uncertainties between the temperature and reddening measurements will usually be correlated. That is why constraints from extinction maps are arguably necessary for our analysis. The third is that the data are slightly offset from the predictions, by a few hundredths of a magnitude, in $(G - J)$, $(J - K_s)$, and $(K_s - W_1)$.

The fourth, and most substantial, conclusion that we derive is that there is an impressive match between the metallicity sensitivity of the color–color relations predicted by the MIST isochrones, and that which can be measured from the GALAH data. That need not have been the case, as the latter are determined by high-resolution spectroscopy, whereas the former are predicted by the product of model atmospheres with estimates of the photometric transmission curves. The qualitative demonstration of this consistency in Figure 2 satisfies two requirements for our methodology to be successful —that broadband colors of stars on the subgiant branch encode some information on metallicity, and that the MIST isochrones reliably predict the trends.

We note that it has long been known that photometry can be incredibly constraining in the inference of stellar parameters (e.g., H. L. Johnson & W. W. Morgan 1953; B. Strömgren 1966; M. Haywood 2002; L. Casagrande et al. 2011). Where this study differs is our emphasis on the subgiant branch to infer ages as well, and the combination of the most widely available ultraviolet through infrared photometry and astrometry for these stars.

3.2. Validation of Astro-photometrically Inferred Metallicities via Comparisons to Spectroscopic Surveys

We compare our astro-photometric metallicity determinations to those from four major spectroscopic surveys in Figure 3. These four surveys are the Gaia High-Resolution Spectrograph Survey (Gaia Collaboration et al. 2023), the APOGEE survey (DR17; S. R. Majewski et al. 2017), the GALAH survey (DR3; S. Buder et al. 2021), and the LAMOST survey (low-resolution spectra (LRS) Data Release 7 (DR7); M. S. Xiang et al. 2015), where we describe our inclusion criteria for these data in our Appendix.

These comparisons validate the assumption that we can in fact reliably infer metallicities over a broad metallicity range, $-2.0 \leqslant$ [Fe/H] $+ 0.50$. Our metallicity inferences are approximately 0.10 dex lower than the spectroscopic values, with a median absolute deviation between the two values of approximately 0.10 dex.

We evaluate the comparison with the GALAH data in greater detail. For those stars, the median offset on the [Fe/H] determinations is 0.08 dex, with a median absolute deviation of 0.08 dex. That median offset is slightly larger than the median reported measurement error in our astro-photometrically derived metallicities (0.06 dex), or the spectroscopically derived metallicities from GALAH (0.07 dex).

In each of the four panels, we see cloud of points with low astro-photometric metallicities but with high spectroscopic metallicities of [Fe/H] $\geqslant -0.50$. For the APOGEE, GALAH, and LAMOST samples we consider it likely that this discrepancy is due to issues with our photometric analysis rather than with the spectroscopic analysis. The reasoning for this is presented in Section 4.4, where we are able to run tests on a larger number of such stars.

3.3. Validation of the Precision and Accuracy of Ages and Metallicities With Well-studied Open Clusters

The open clusters M67 (NGC 2682) and NGC 188 are well studied, and thus provide an independent means to validate our methodology to infer ages and metallicities. We can evaluate if our parameter inferences for subgiant stars within a cluster are consistent with one another as a proxy for precision, and if they are consistent with other literature values as a proxy for accuracy.

3.3.1. Empirical Population Parameters for the Validation Clusters

All literature references for cluster parameters that either inform our choice of priors or the evaluation of our results are listed in Table 1.

For the distances to the clusters, we assume the inverse of the parallax values that have been vetted by the Gaia collaboration (Gaia Collaboration et al. 2018a). Both parallaxes are precisely measured ($\pi/\sigma_\pi \geqslant 100$), and we shift the parallaxes by a zero-point offset of $\delta_\pi = 0.054$ mas, such that the parallaxes are increased (R. Schönrich et al. 2019). In contrast, if we used the parallax measurements for each individual stars, we would

[6] https://isochrones.readthedocs.io/en/latest/
[7] https://waps.cfa.harvard.edu/MIST/model_grids.html#bolometric

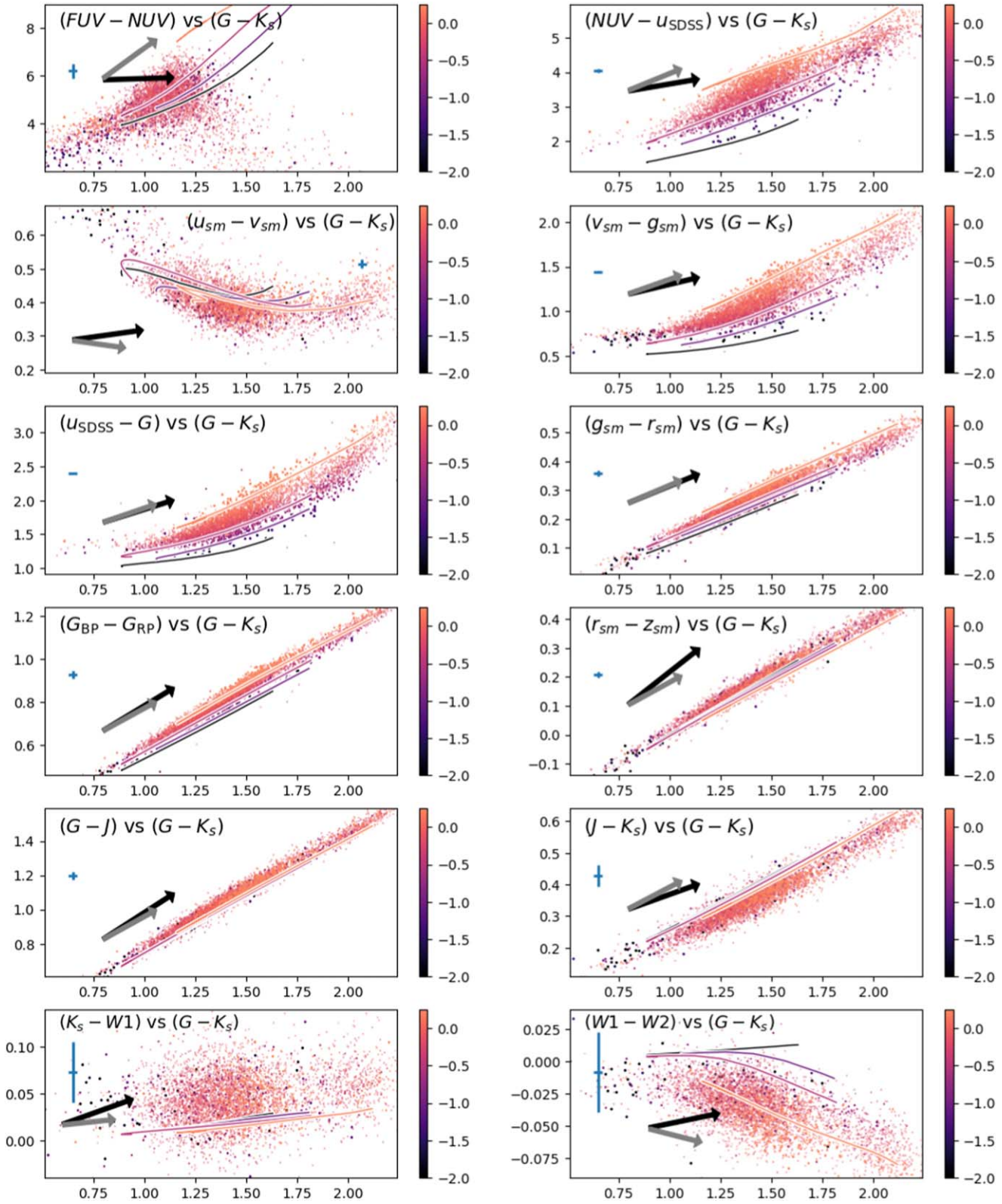

Figure 2. We show various photometric scatters for stars on or near the subgiant branch. The [Fe/H] measurements (S. Buder et al. 2021) are color coded, as are the predictions from the MIST isochrones. The effects of increasing the extinction by $\Delta A_V = 0.50$ mag and $\Delta T_{\rm eff} = 500\ K$ are approximated by the black and gray arrows, respectively, and representative photometric uncertainties are shown by the cyan error bars. The association between the spectroscopically inferred metallicities and color–color relations is consistent with the theoretical prediction.

have a median precision of $\pi/\sigma_\pi \approx 70$ for M67 and $\pi/\sigma_\pi \approx 30$ for NGC 188, and thus the parameter inferences would be degraded relative to most of our sample.

For the extinction to these clusters, the Pan-STARRS reddening maps (G. M. Green et al. 2019) would be the ideal choice for reddening estimates, as using these values would

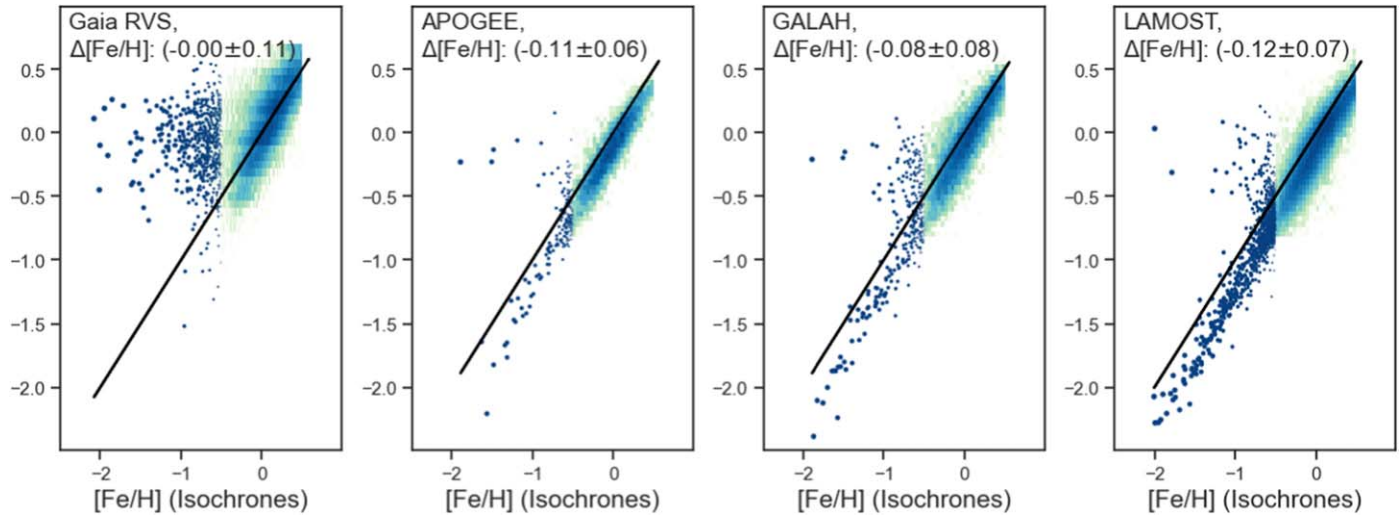

Figure 3. A comparison between our astro-photometric metallicity determinations and those from four major spectroscopic surveys. Legends show the median difference in [Fe/H], where a positive value denotes a higher metallicity for the spectroscopic determination, and the median absolute deviation between the metallicity determinations. The black lines denote the lines of equality between the metallicity determinations. This comparison to data from four surveys demonstrates that our astro-photometric estimates of metallicity are largely consistent with the spectroscopically inferred values.

Table 1
Literature References as Well as the Estimates in This Work for the Population Parameters of the Clusters

Population	Parallax (mas)	[Fe/H]	log(Age)	A_V	Reference and Comments
M67	1.1865 ± 0.0011	⋯	⋯	⋯	Gaia Collaboration et al. (2018a), R. Schönrich et al. (2019)
M67	⋯	+0.01	⋯	⋯	U. Heiter et al. (2014)
M67	⋯	+0.00	⋯	⋯	F. Liu et al. (2019)
M67	⋯	+0.03	⋯	⋯	L. Casamiquela et al. (2019)
M67	⋯	+0.01	⋯	⋯	J. Donor et al. (2020)
M67	⋯	+0.00	⋯	⋯	L. Spina et al. (2021)
M67	⋯	⋯	9.32	⋯	N. V. Kharchenko et al. (2013)
M67	⋯	⋯	9.63	⋯	T. Cantat-Gaudin et al. (2020)
M67	⋯	⋯	9.54	⋯	D. Stello et al. (2016)
M67	⋯	⋯	9.63	⋯	F. Liu et al. (2019)
M67	⋯	⋯	9.57	⋯	E. L. Sandquist et al. (2021)
M67	⋯	⋯	⋯	0.124	A. Sarajedini et al. (1999)
M67	⋯	⋯	⋯	0.186	N. V. Kharchenko et al. (2005)
M67	⋯	⋯	⋯	0.186	A. K. Pandey et al. (2010)
M67	⋯	⋯	⋯	0.27	S. Meibom et al. (2009)
M67	⋯	⋯	⋯	0.127	B. J. Taylor (2007)
M67	⋯	⋯	⋯	0.109	L. Viani & S. Basu (2017)
M67	⋯	⋯	⋯	0.093	Y. H. M. Hendy & H. I. Abdel Rahman (2022)
M67	⋯	⋯	⋯	0.248	D. A. VandenBerg et al. (2007)
NGC 188	0.5593 ± 0.0011	⋯	⋯	⋯	Gaia Collaboration et al. (2018b), Schönrich et al. (2019)
NGC 188	⋯	+0.11	⋯	⋯	U. Heiter et al. (2014)
NGC 188	⋯	+0.03	⋯	⋯	L. Casamiquela et al. (2019)
NGC 188	⋯	+0.09	⋯	⋯	J. Donor et al. (2020)
NGC 188	⋯	+0.09	⋯	⋯	L. Spina et al. (2021)
NGC 188	⋯	⋯	9.65	⋯	N. V. Kharchenko et al. (2013)
NGC 188	⋯	⋯	9.85	⋯	T. Cantat-Gaudin et al. (2020)
NGC 188	⋯	⋯	9.84	⋯	X. Chen et al. (2016)
NGC 188	⋯	⋯	⋯	0.279	A. Sarajedini et al. (1999)
NGC 188	⋯	⋯	⋯	0.248	A. K. Pandey et al. (2010)
M67	1.1897 ± 0.0007	0.04 ± 0.08	9.58 ± 0.04	0.12 ± 0.01	Derived means and weighted standard deviations
M67	1.1865 ± 0.0000	0.03 ± 0.05	9.60 ± 0.01	0.12 ± 0.00	Medians and median absolute deviations
M67 (M. Xiang & H.-W. Rix 2022)	⋯	-0.11 ± 0.05	9.63 ± 0.03	⋯	Derived means and standard deviations
M67 (M. Xiang & H.-W. Rix 2022)	⋯	-0.11 ± 0.02	9.61 ± 0.02	⋯	Medians and median absolute deviations
NGC 188	0.5593 ± 0.0000	0.11 ± 0.18	9.79 ± 0.08	0.26 ± 0.03	Derived means and standard deviations
NGC 188	0.5593 ± 0.0001	0.13 ± 0.06	9.80 ± 0.03	0.26 ± 0.06	Medians and median absolute deviations

Note. Where references report reddening in terms of $E(B-V)$, we multiply their values by $A_V/E(B-V) = 3.1$. The inclusion criteria for cluster stars in terms of photometry and indicators of (non)variability are the same as they are for stars in the main sample, yielding 20 stars in M67 and 34 stars in NGC 188.

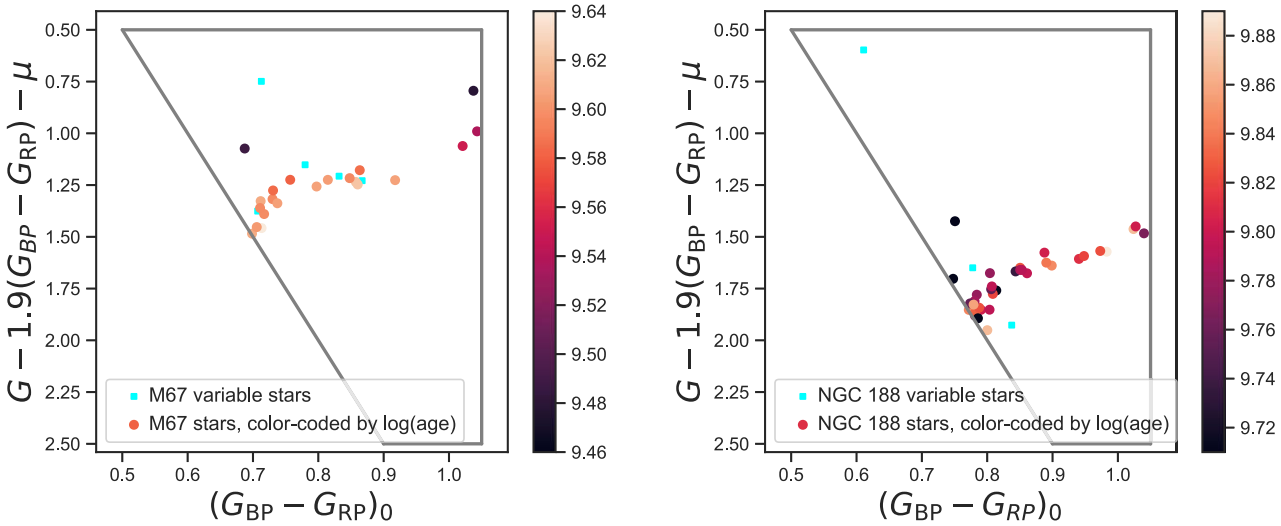

Figure 4. Color–magnitude diagrams of stars in M67 (left) and NGC 188 (right) color coded by the derived age, with the stars identified as variable or otherwise less reliable shown as cyan squares. Our analysis finds very little dispersion in the derived ages among the subgiant branch stars, but there is some contamination from stars that are likely to be blue stragglers.

provide the most consistency with the rest of our work. However, we have found that these estimates are unphysically noisy toward clusters, varying by a factor of several among the cluster stars. That may be because of confusion affecting some of the photometry used to construct those maps, or because a pileup of stars at a specific distance radically violates the smooth priors on the distribution of stars in the Milky Way assumed in the construction of those maps (G. Green, private communication). We instead use the inferences $A_{V,\mathrm{M67}} = 0.120 \pm 0.012$ and $A_{V,\mathrm{NGC\ 188}} = 0.260 \pm 0.026$ as part of our likelihood, with the priors on the extinction modified as they are for stars in the main sample.

Literature and age estimates of the metallicities of these clusters vary. For these parameters, we assume the same priors as we do for the stars in the main sample, a flat prior in metallicity over the range $-2.0 \leqslant [\mathrm{Fe/H}] \leqslant +0.50$, and a flat prior in log(age) over the range $1.0 \leqslant \tau/\mathrm{Gyr} \leqslant 13.721$. As elsewhere, we assume a Chabrier prior in the initial stellar mass over the range $0.70 \leqslant M/M_{\odot} \leqslant 2.0$

The inclusion criteria for cluster stars in terms of photometry and indicators of (non)variability are the same as they are for stars in the main sample, yielding 20 stars in M67 and 34 stars in NGC 188.

3.3.2. Ages of Cluster Subgiants: Trends and Results

Our results for stars associated with M67 and NGC 188 are summarized at the bottom of Table 1, and the dependence of age on location in the color–magnitude diagram is shown in Figure 4.

The derived metallicities and ages are consistent with the literature values, and consistent with one another. For M67, the median absolute deviation and 1σ precision in ages and metallicities are 3% and 9%, and 0.05 and 0.08 dex, respectively. For NGC 188, the median absolute deviation and 1σ precision in ages and metallicities are 6% and 19%, and 0.06 and 0.18 dex, respectively.

For both clusters, the median absolute deviations in the ages are substantially smaller (≈70%) than the weighted standard deviations, where we would only expect them to be ≈33% smaller for normally distributed errors. That is because the distributions of derived parameters have a high kurtosis as the ends of the distributions are dominated by outliers. The nature of those outliers are easy to identify in Figure 4—our variability criteria can flag many, but not all, of the stars that are binaries, products of binary evolution, etc. There may also be some field star contamination, even after selecting for stars using proper motions.

The subgiant stars in NGC 188 are ≈3× less likely to be identified as variables than those in M67—and that is not surprising, as some of of our variability criteria will be less effective for stars at the greater distance of NGC 188 (1788 versus 843 pc). The brightest unflagged bright subgiant stars in M67 and NGC 188, which may very well be blue stragglers, have derived ages of log(age) = 9.48 and log(age) = 9.64, respectively. These stars add to the dispersion in the derived parameters of these clusters in a manner that will be less likely for nearby field stars.

A key limitation of this comparison, as pointed out by the anonymous referee, is that stellar isochrones and the stellar physics that go into them have been evaluated and even calibrated by comparison to clusters, and thus these comparisons are not necessarily independent. In this particular case, J. Choi et al. (2016) actually fit for a key parameter of stellar models, the convective overshoot for stellar cores, by comparing the shape of the main-sequence turnoff in M67 to the predictions. They derived $f_{\mathrm{ov,core}} = 0.016$.

3.4. Comparison to the Results of M. Xiang & H.-W. Rix (2022)

The work of M. Xiang & H.-W. Rix (2022) is arguably the most similar comparison that we have to our own investigation. They too, sought to use the tremendous diagnostic power of Gaia astrometry to estimate the ages of subgiant branch stars, and by extension, of the solar neighborhood as a whole. There are several differences in our methodologies, most particularly.

1. For the most effective constraint on metallicity, our investigation requires an ultraviolet flux measurement, whereas that of M. Xiang & H.-W. Rix (2022) required a LAMOST spectrum and subsequently derived stellar parameters.

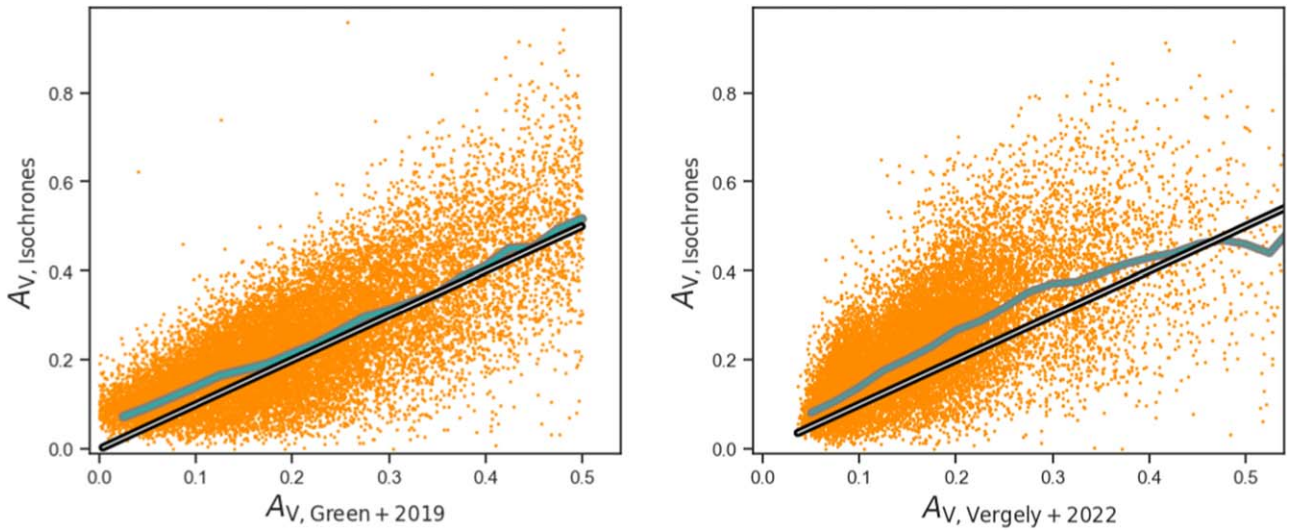

Figure 5. Comparison of our derived extinction values relative to those of the G. M. Green et al. (2019) maps (left) and the J. L. Vergely et al. (2022) maps (right). The black and white lines denote equality, and the blue line denotes the median trends. Both maps do well in the mean, but the predictions of G. M. Green et al. (2019) fare better for $A_V \gtrapprox 0.10$, which comprise the majority of our primary sample.

2. Our method estimates a mean total metallicity as "[Fe/H]" whereas that of M. Xiang & H.-W. Rix (2022) splits the metallicity into [Fe/H] and [α/Fe] parameters. The latter approach comes with the "cost" of an extra free parameter, but it is one which is physically well motivated and constrained by the LAMOST spectra. The impact of accounting for [α/Fe] is shown in the right panel of Supplementary Figure 4 of M. Xiang & H.-W. Rix (2022): isochrones that underestimate [α/Fe] by 0.20 dex will overestimate ages by approximately 1.5 Gyr in the mean, but that is in the case where [Fe/H] is fixed to the spectroscopic value. In our case, we infer an "effective" [Fe/H] value, which will be shifted for α-enhanced stars.
3. Both methods derive A_V from available extinction maps, predominantly that of G. M. Green et al. (2019) in this investigation and entirely from that of M. Xiang & H.-W. Rix (2022). However, our method assumes a constant total-to-selective extinction ratio $R_V = A_V/E(B-V) = 3.1$, whereas that of M. Xiang & H.-W. Rix (2022) varies R_V for every star as an additional free parameter.
4. The two investigations have different variability exclusion criteria, which are too numerous to fully describe here.

There are 31,876 stars in common between our two samples, including 29,965 that satisfy our sample's variability and blending criteria. Among those, our derived [Fe/H] values are systematically higher, with Δ[Fe/H] $\sim 0.19 \pm 0.10$, and our derived ages are systematically lower, with the age ratio distributed as $\tau_{\rm This\ Work}/\tau_{\rm Xiang} \sim 0.94 \pm 0.13$.

A diagnostically powerful point of comparison is that of the open cluster M67, for which there are numerous available literature benchmark measurements. Our sample includes 20 M67 members, that of M. Xiang & H.-W. Rix (2022) includes seven member stars, and there are four stars in common between our two samples. Of the three that do not make it into our sample, two are excluded because they are bluer than our subgiant selection cutoff, and one is excluded due to the absence of an ultraviolet photometric measurement.

Regardless of whether or not we select the four stars in common or the seven total M67 stars in their sample, M. Xiang & H.-W. Rix (2022) infer a slightly higher mean age for M67, and a slightly lower mean metallicity. The respective ratio (95%) and offset (0.14 dex) are effectively identical to that for for our samples as a whole.

We conclude our two samples are consistent, showing that ultraviolet photometry and large-survey spectroscopy currently have comparable diagnostic power for the inferences of ages and metallicities of subgiant branch stars.

3.5. Validations of the Assumed Extinction Maps

In this investigation we assume the extinction maps of G. M. Green et al. (2019), and R. Lallement et al. (2022) and J. L. Vergely et al. (2022). When extinction estimates from both maps are available, we prioritize those from the former. Where only measurements from the latter are available, we transform them using the prescription in item #8 of the list in Section 2.3, which we derive here.

Here, we seek to assess the validity of those assumptions as follows. We use a subsample of stars for which we have an extinction estimate from both reddening maps, for which GALEX NUV is measured to a precision of better than 0.10 mag, and for which there is also an ultraviolet measurement from either Skymapper or SDSS. That yields a sample of 18,176 stars.

For those stars, the combination of both NUV and u photometry should enable us to reliably estimate extinction from the photometry and astrometry alone. We thus remove the extinction measurements from the likelihood, and relax the prior to being a flat prior in the range $A_V \in [0,\ A_{V,\rm Green} + A_{\rm V,Vergely} + 0.05]$.

For this sample, we find that the extinction maps of G. M. Green et al. (2019) fare better than those of J. L. Vergely et al. (2022) in the mean offsets, with offsets of $A_{V,\rm Maps} - A_{\rm V,Inferred}$ of 0.035 ± 0.092 versus 0.066 ± 0.100, respectively. Here the errors denote 1σ dispersions. The distributions are shown in Figure 5.

That may however be an artifact of our sample—we notice, for example, that the maps of J. L. Vergely et al. (2022) fare

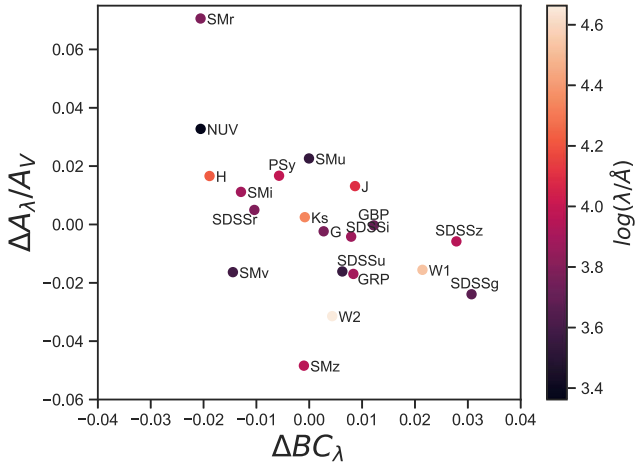

Figure 6. The scatter of the derived errors of the mean extinction coefficients as a function of the derived mean errors in the bolometric corrections, color coded by filter effective wavelength. The fact that the two variables are anticorrelated is indicative of undiagnosed systematic errors, such as errors in the assumed filter transmission curves.

better than those of G. M. Green et al. (2019) for lower values of the inferred extinction. If we restrict the comparison to $A_{V,\mathrm{Inferred}} \leqslant 0.10$, the mean offsets are 0.024 ± 0.058 and 0.038 ± 0.079 mag, respectively.

3.6. Validation of the Assumed Bolometric Coefficients and Extinction Curve

The uncertainties of the assumed bolometric corrections and interstellar extinction curves are among the most obvious contributors to the uncertainty in photometric investigations such as this one.

In order to estimate the magnitude of this uncertainty, we construct a subsample of 5558 stars which have (i) a GALEX NUV magnitude with measurement precision better than 0.10 mag; (ii) a u-band measurement; (iii) a precision in extinction from G. M. Green et al. (2019) that is better than 10%; and (iv) a metallicity measurement from LAMOST with $[\mathrm{Fe/H}] \leqslant +0.35$. For the latter, we then assume a metallicity measurement of $[\mathrm{Fe/H}] = [\mathrm{Fe/H}]_{\mathrm{LAMOST}} + 0.12$ in our likelihood (see Figure 3), and we inflate all photometric uncertainties by 0.05 mag in quadrature, rather than the 0.01 mag used elsewhere in this text.

Then, for each bandpass X, we plot the scatter of $X_{\mathrm{Predicted}} - X_{\mathrm{Measured}}$ as a function of A_V, and compute the least squares linear fit. We then show the slopes as a function of the intercepts for each bandpass in Figure 6.

In principle, this should be a scatter of the errors in the extinction coefficients $\Delta A_X/A_V$ as a function of the errors in the bolometric corrections $\Delta \mathrm{BC}_X$ for each bandpass X, but in practice we see that this is unlikely to be the case. The two variables are anticorrelated, with a Spearman coefficient of $\rho = -0.53$ and a p-value of $p = 0.02$. We consider this anticorrelation to be indicative of small, undiagnosed systematic errors.

Another way to discern the presence of such errors is that the coefficients for bandpasses of similar effective wavelengths, denoted by similar color coding in Figure 6, do not yield the same derived errors in the extinction coefficients. For example there is a 0.04 mag offset in $\Delta A_X/A_V$ between u_{SDSS} and u_{SM}, and a 0.07 mag offset in $\Delta A_X/A_V$ between r_{SDSS} and r_{SM}, when those offsets should be close to 0 on physical grounds. Separately, it is known that there is an uncertainty of 1%–5% in the zero-points of the GALEX filters (M. H. Siegel et al. 2010), which should be reduced for upcoming ultraviolet observatories such as ULTRASAT (Y. Shvartzvald et al. 2024) and UVEX (S. R. Kulkarni et al. 2021).

Regardless of these issues, it is at least the case that the offsets are small. The median of the absolute values of the offsets in the bolometric corrections and the extinction coefficients are given by $\Delta \mathrm{BC}_X = 0.010$ and $\Delta A_X/A_V = 0.016$, respectively. The latter's impact is further reduced due to the fact that the median extinction of our primary sample is $A_V \approx 0.15$ mag.

At this time, we cannot reliably discern if these offsets are due to the photometric data reduction or in the predictions of the stellar models, but this may become feasible as more data become available, in particular data from different observatories measuring photometry in nominally similar bandpasses. Given these uncertainties, we choose not to investigate the effects of possible sight-line-dependent variations in the interstellar extinction curve, which can bias the derived parameters of stars if not adequately accounted for (H. Roussel et al. 2005; M. Gennaro et al. 2012; D. M. Nataf 2015, 2021; D. An et al. 2024; E. Bica et al. 2024).

3.7. Sensitivity of the Derived Parameters to the Input Data and Priors

Here, we evaluate the sensitivity of our derived stellar parameters as a function of the input data and priors. For the tests following the first one, we use a randomly selected sample of approximately 5000 stars selected to have $\pi/\sigma_\pi \geqslant 100$ and $\sigma_{A_V} \leqslant 0.05$. We list the effects of these changes in approximately decreasing order of the size of their effects.

3.7.1. The Effect of Removing the Ultraviolet Measurements from the Likelihood

We evaluate the effect of removing the measurements of NUV, u_{SM}, v_{SM}, and u_{SDSS} from the likelihood. The mean offset in metallicity, where we report the catalog value subtracted from the adjusted value, is $\Delta[\mathrm{Fe/H}] = -0.02 \pm 0.17$, and similarly, $\Delta \log(\mathrm{age}) = -0.00 \pm 0.06$. The Pearson correlation between these two offsets is $\rho = -0.81$.

Thus, in the mean, removing the ultraviolet measurements negligibly biases the results, but it does yield a very large and very correlated statistical error for the derived ages and metallicities.

3.7.2. The Effect of Removing the Extinction Priors from the Likelihood and Adjusting Them in the Prior

We evaluate the effect of removing the available measurements of extinction from both the likelihood and priors, and replacing them with a flat prior in A_V over the range [0, 1].

The mean offset in metallicity, where we report the catalog value subtracted from the adjusted value, is $\Delta[\mathrm{Fe/H}] = -0.07 \pm 0.08$, and similarly, $\Delta \log(\mathrm{age}) = 0.08 \pm 0.11$. The Pearson correlation between these two offsets is $\rho = -0.72$.

3.7.3. The Effect of Removing Both the 2MASS and WISE Data from the Likelihood

We evaluate the effect of removing the measurements of J, H, K_s, W_1, and W_2 from the likelihood.

The mean offset in metallicity, where we report the catalog value subtracted from the adjusted value, is $\Delta[\mathrm{Fe/H}] = 0.02 \pm 0.08$, and similarly, $\Delta \log(\mathrm{age}) = -0.02 \pm 0.06$. The Pearson correlation between these two offsets is $\rho = -0.70$.

3.7.4. The Effect of Removing the WISE Data from the Likelihood

We evaluate the effect of removing the measurements of W_1 and W_2 from the likelihood.

The mean offset in metallicity, where we report the catalog value subtracted from the adjusted value, is $\Delta[\mathrm{Fe/H}] = -0.01 \pm 0.02$, and similarly, $\Delta \log(\mathrm{age}) = 0.01 \pm 0.02$. The Pearson correlation between these two offsets is $\rho = -0.46$.

3.7.5. The Effect of Adjusting the Prior on the Metallicity

We evaluate the effect of changing our metallicity prior, which is a flat prior in metallicity, over the internal range $-2.0 \leqslant [\mathrm{Fe/H}] \leqslant +0.50$, to the default prior suggested by isochrones. The default prior has a dominant peak near $[\mathrm{Fe/H}] = 0$, with a long tail to lower metallicities.[8]

The mean offset in metallicity, where we report the catalog value subtracted from the adjusted value, is $\Delta[\mathrm{Fe/H}] = 0.01 \pm 0.02$, and similarly, $\Delta \log(\mathrm{age}) = 0.00 \pm 0.02$. The Pearson correlation between these two offsets is $\rho = -0.65$. Approximately 5% of the sample stars have changes in either [Fe/H] or log(age) exceeding 0.05 dex, and approximately 1% of the sample stars have changes exceeding 0.10 dex. These shifts in the derived parameters are represented by the errors: whereas the stars whose derived values of log(age) shifted by less than 0.05 had mean errors in their ages of 9.3%, those for which log(age) shifted by more than 0.05 had mean errors in their ages of 28.4%.

3.7.6. The Effect of Increasing or Decreasing the Number of Live Points Used in the Nested Sampling

We evaluate the effect of increasing the number of live points used by MultiNest for the fitting, from 1000 to 3000 live points, and then from 1000 to 300 live points.

When we increase the number of live points to 3000, the shift in the mean offset in metallicity, where we report the catalog value subtracted from the adjusted value, is $\Delta[\mathrm{Fe/H}] = 0.00 \pm 0.00$, and similarly, $\Delta \log(\mathrm{age}) = 0.00 \pm 0.01$. The largest change in the derived value of [Fe/H] is 0.03 dex. For the derived values of log(age), some 0.2% of the stars have parameter shifts of more than 0.05 dex, with the largest recorded shift being 0.08 dex.

Similar results are obtained when we decrease the number of live points to 300, where the shift in the mean offset in metallicity, where we report the catalog value subtracted from the adjusted value, is $\Delta[\mathrm{Fe/H}] = 0.00 \pm 0.00$, and similarly, $\Delta \log(\mathrm{age}) = 0.00 \pm 0.01$. The largest change in the derived value of [Fe/H] is 0.04 dex. For the derived values of log(age), some 0.6% of the stars have parameter shifts of more than 0.05 dex, with the largest recorded shift being 0.11 dex.

[8] The default priors for the isochrones package are described more fully at https://isochrones.readthedocs.io/en/latest/starmodel.html#Priors.

4. Main Results

4.1. Availability of the Derived Parameters and the Uncertainties Thereof

The table of derived stellar parameters (16th, 50th, and 84th percentiles of the posteriors) of our program stars can be found in Table 2 of the online edition of this paper.

The input tables for the 401,819 stars in the primary sample and the metal-poor annex, including the crossmatches to other surveys, the Python Jupyter Notebook used to evaluate them, associated readme file, and links to the table of derived parameters can be found in a github repository of this paper's first author[9] and in the Zenodo repository doi:10.5281/zenodo.13750877.

The data that support the findings of this study are openly available in the Johns Hopkins Research Data Repository at doi:10.7281/T1/CGBG4F. It includes the abovementioned data, as well as the full probabilistic posteriors for the derived stellar parameters (e.g., [Fe/H], A_V, etc.) of each star.

4.2. Primary Sample: Ages and Metallicities

We show, in the right panel of Figure 7, the distribution in age–metallicity space for 242,489 stars from our primary sample which are not associated with open clusters, and which satisfy our other inclusion criteria.

We observe three age–metallicity components in our sample. The first is an excess concentration centered at $(\tau/\mathrm{Gyr}, [\mathrm{Fe/H}]) \approx (4, 0)$, corresponding to the age and metallicity of the Sun. The second excess concentration is centered at $(\tau/\mathrm{Gyr}, [\mathrm{Fe/H}]) \approx (7, +0.15)$, and the third is a streak of stars distributed along a narrow band in age–metallicity space, from $(\tau/\mathrm{Gyr}, [\mathrm{Fe/H}]) \approx (8, +0.15)$ to $(13, -0.50)$. Not one of these three features would be discernible if we were to look at either of the marginal distributions of age and [Fe/H] distributions, but they are easily discernible in the joint distribution of age and metallicity.

We have verified that the presence of these three components is robust to the following methodological changes: requiring an uncertainty in A_V of less than 0.05 mag; requiring a low inferred value for the extinction of $A_V \leqslant 0.20$; requiring either a detection or nondetection in NUV; requiring a detection in v_{SM}; requiring an inferred distance of less than 500 parsecs; and finally, requiring an age precision of better than 7%.

We also comment on the ends of our parameter space. First, the fact that we barely detect any stars with $\tau/\mathrm{Gyr} \leqslant 2$ is due to our color–magnitude selection function (see Figure 1). Second, the lack of stars with $[\mathrm{Fe/H}] > 0.50$ is due to that being the end of the MIST isochrone grid, and likely as well the fact that those stars are intrinsically rare. Finally, we have a reassuringly small excess of stars with $\tau/\mathrm{Gyr} \approx 13.7$. That is a cosmologically motivated end to our allowed parameter space, nevertheless, we would expect to see a large pileup of stars at old ages if either of our measurement or methodological errors were larger, for example if we frequently and significantly underestimated reddening or metallicity. Though there is a pileup that can be seen at the right end of the left panel of Figure 7, it is reassuringly small.

We estimate our selection bias as follows. First, we require the stars to have predicted photometric parameters satisfying those in the top panel of Figure 1. We then require that the star

[9] https://github.com/DavidMoiseNataf/Subgiants

Table 2
Summary Input Data and the Derived Stellar Parameters for 401,819 Stars

Num	Label	Explanations
1	dr3_source_id	Unique source identifier in Gaia DR3 (Gaia Collaboration et al. 2023), for all sample stars
2	objid_GALEX	Unique source identifier in GALEX (L. Bianchi et al. 2017) if in catalog, otherwise null
3	R.A.	R.A. from Gaia DR3, Epoch J2016
4	decl.	decl. from Gaia DR3, Epoch J2016
5	ra2000	R.A. from Gaia DR3, Epoch J2000
6	dec2000	decl. from Gaia DR3, Epoch J2000
7	l2000	Galactic longitude from Gaia DR3, Epoch J2000
8	b2000	Galactic latitude from Gaia DR3, Epoch J2000
9	phot_g_mean_mag	*G*-band mean magnitude from Gaia DR3
10	mass_16	16th percentile of the posterior distribution of the initial stellar mass
11	mass	50th percentile of the posterior distribution of the initial stellar mass
12	mass_84	84th percentile of the posterior distribution of the initial stellar mass
13	age_16	16th percentile of the posterior distribution of the stellar age
14	age	50th percentile of the posterior distribution of the stellar age
15	age_84	84th percentile of the posterior distribution of the stellar age
16	feh_16	16th percentile of the posterior distribution of the stellar metallicity
17	feh	50th percentile of the posterior distribution of the stellar metallicity
18	feh_84	84th percentile of the posterior distribution of the stellar metallicity
19	AV_model_16	16th percentile of the posterior distribution of the extinction to the star A_V
20	AV_model	50th percentile of the posterior distribution of the extinction to the star A_V
21	AV_model_84	84th percentile of the posterior distribution of the extinction to the star A_V
22	Teff_16	16th percentile of the posterior distribution of the stellar surface effective temperature $T_{\rm eff}$
23	Teff	50th percentile of the posterior distribution of the stellar surface effective temperature $T_{\rm eff}$
24	Teff_84	84th percentile of the posterior distribution of the stellar surface effective temperature $T_{\rm eff}$
25	logg_16	16th percentile of the posterior distribution of the stellar surface gravity $\log g$
26	logg	50th percentile of the posterior distribution of the stellar surface gravity $\log g$
27	logg_84	84th percentile of the posterior distribution of the stellar surface gravity $\log g$
28	GP_Jp	Azimuthal action, all dynamical variables derived by `galpy` (J. Bovy 2015)
29	GP_Jr	Radial action
30	GP_Jz	Vertical action
31	GP_Lz	Orbital angular momentum about the Galactic major axis
32	GP_E	Energy of orbit, negative for bound orbits
33	GP_Rperi	Smallest distance to Galactic center of orbit
34	GP_Rap	Largest distance to Galactic center of orbit
35	GP_zmax	Largest separation from the plane of orbit
36	GP_ecc	Eccentricity of orbit
37	Blend	"1" for stars for which photometry appears blended as per the criteria of Section 2.1, "0" otherwise
38	Chance_pvalue	*p*-value from Q. Chance et al. (2022) if measured, otherwise null
39	VarExcess	Percentile of photometric variability in Gaia *G* band with respect to the rest of the sample
40	Sample	"PS" for primary sample, "MPannex" for metal-poor annex

Note. Summary input data and derived parameter for 401,819 subgiants. This table is published in its entirety in the machine-readable format in the online edition. (This table is available in its entirety in machine-readable form in the online article.)

either have a predicted $14 \leqslant \mathrm{NUV} \leqslant 22$, $12 \leqslant u_{\rm SDSS} \leqslant 17$, or $11 \leqslant u_{\rm SM} \leqslant 17$, as is the case for the stars in our sample, given a volumetrically uniform distribution satisfying $250 \leqslant d/\mathrm{pc} \leqslant 1000$. This approximation of the selection probability, shown in Figure 8, varies little for stars with $2 \leqslant \tau/\mathrm{Gyr} \leqslant 12$ and $-1.0 \leqslant [\mathrm{Fe/H}] \leqslant +0.50$. As these stars comprise the vast majority of our sample, the selection function has little effect on our final sample.

There are certainly factors not included in the estimate of our selection function that could significantly adjust the selection probability. These include a possible age and metallicity dependence to the detectable binary fraction, the correlations between the spatial selection functions of GALEX, SDSS, and Skymapper and the metallicity distribution functions of field stars, and the correlation between high-extinction sight lines (which tend to be along the Galactic plane) and the age–metallicity distributions of those sight lines. The computation of these adjustment factors would constitute a large study of their own, and are thus beyond the scope of this investigation.

4.3. The Associations Between the Derived Ages and Dynamics

We estimate the dynamical properties of our sample stars using `galpy`[10] (J. Bovy 2015), and compute the orbits using the module developed by J. T. Mackereth & J. Bovy (2018). Some of our results may be inverted relative to other studies as `galpy` uses a left-handed Galactocentric coordinate frame.

We adopted the `MWPotential2014` described by J. Bovy (2015). In that model, the bulge is parameterized as a power-law density profile that is exponentially cut off at 1.9 kpc with a power-law exponent of −1.8. The disk is represented by a Miyamoto–Nagai potential with a radial scale length of 3 kpc and a vertical scale height of 280 pc (M. Miyamoto &

[10] http://github.com/jobovy/galpy

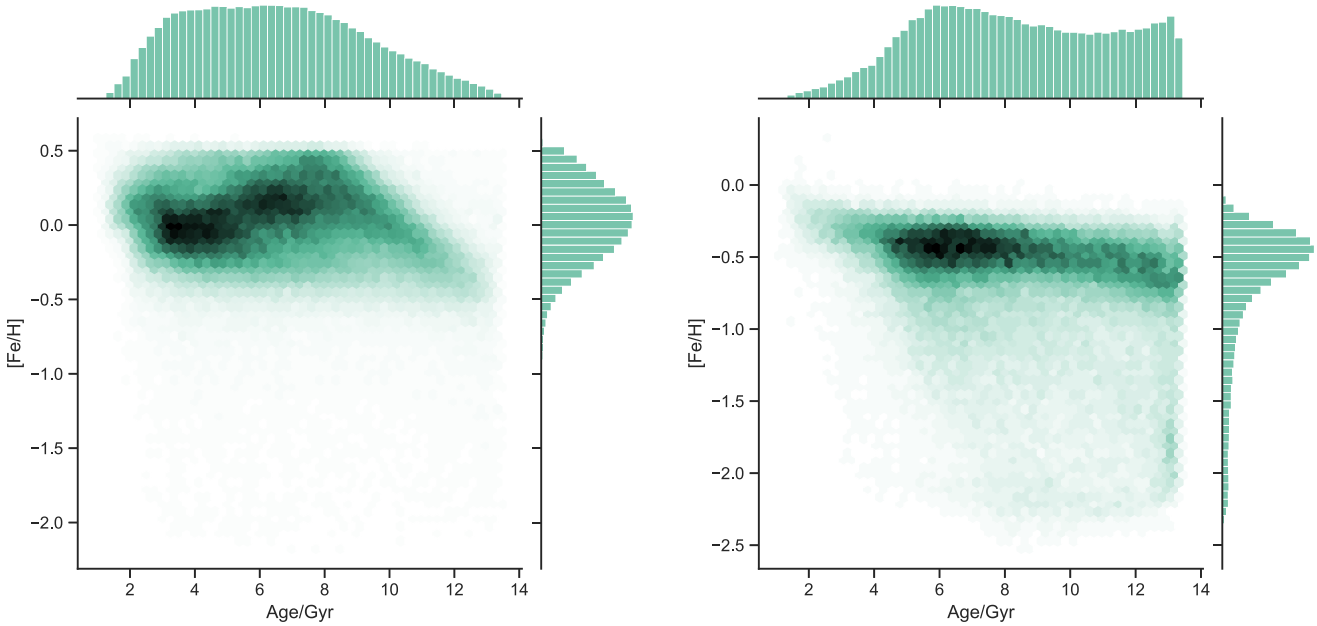

Figure 7. Left: the distribution in age–metallicity space for 242,489 stars from our primary sample which are not associated with open clusters, and which satisfy our other variability and blending inclusion criteria. Right: the distribution in age–metallicity space for 96,247 stars from our metal-poor annex which are not associated with open clusters, and which satisfy our other variability and blending inclusion criteria. The age–metallicity distribution functions show considerable structure that would not be discernible in either of the marginal distributions.

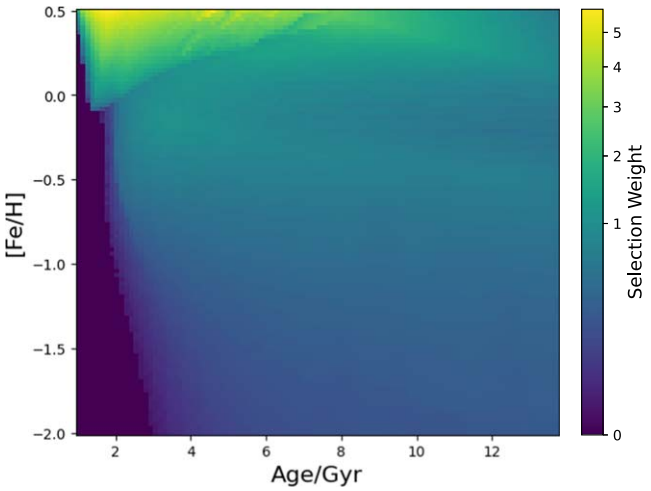

Figure 8. An approximation of our selection function as a function of age and metallicity, where the selection weight is normalized to 1 for a star of solar age and metallicity. The selection function is close to uniform in the age–metallicity regime where stars are found in numerous numbers.

R. Nagai 1975). The halo is modeled as a Navarro–Frenk–White halo with a scale length of 16 kpc (J. F. Navarro et al. 1996). We set the solar distance to the Galactic center to $R_0 = 8.122$ kpc (GRAVITY Collaboration et al. 2018), the circular velocity at the Sun to $V_0 = 238$ km s^{-1} (R. Schönrich 2012; J. Bland-Hawthorn & O. Gerhard 2016), the height of the Sun above the plane to $z_0 = 25$ pc, and the solar motion with the respect to the local standard of rest to ($U_\odot$, $V_\odot$, $W_\odot$) = (10.0, 11.0, 7.0) km s^{-1} (M. Jurić et al. 2008), where the latter is consistent with the values of ($U_\odot$, $V_\odot$, $W_\odot$) = (11, 12, 7) km s^{-1} derived by R. Schönrich et al. (2010).

In Figure 9, we show the distribution of estimated orbital parameters for 105,445 sample stars with derived ages that are estimated to be precise to 7% or better. The distribution in action space is shown in the two left columns, and in the right column we show the distribution as a function of two integrals of motion (energy and angular momentum around the Galaxy's rotation axis). As our assumed gravitational potential for the Milky Way is axisymmetric, the action J_ϕ is exactly equal to the angular momentum L_z. Then, in Figure 10, we show the distribution of stars of our combined sample (including the metal-poor annex) as a function of E versus L_z, binned by age and metallicity.

What we find is that the older stars are broadly distributed in dynamical space, meaning older stars can in fact be found in any region of dynamical phase space where we find any stars at all. The trend is for the dynamical distribution of stars to become more and more localized as the derived ages of stars become younger and younger. This result is qualitatively consistent with the Milky Way Disk formation model of R. Schönrich & J. Binney (2009), who postulated that the thick and thin disks were born at the same time. That is in contrast to various other observational arguments that the oldest thick disk is several gigayears older than the oldest thin disk stars (e.g., M. Haywood 2008; M. Kilic et al. 2017). There is evidence previously discussed in the literature of ancient stars on thin disk orbits, but these have thus far been few and far between (G. R. Ruchti et al. 2011; K. C. Schlaufman et al. 2018), though this subject appears to be on the ascendancy (M. Bellazzini et al. 2024; J. Hong et al. 2024; H. Zhang et al. 2024). To the best of our knowledge, ours is the first analysis of a sample of these stars for which precise ages are available.

4.4. The Metal-poor Annex

We constructed the metal-poor annex, using the criteria delineated in Section 2, so as to extract a sample of metal-poor subgiant stars. These are indistinguishable from the vastly more numerous metal-rich turnoff stars on the optical color–magnitude diagram, but can be selected statistically using a combination of ultraviolet and optical colors, as can be better understood by inspecting Figure 2.

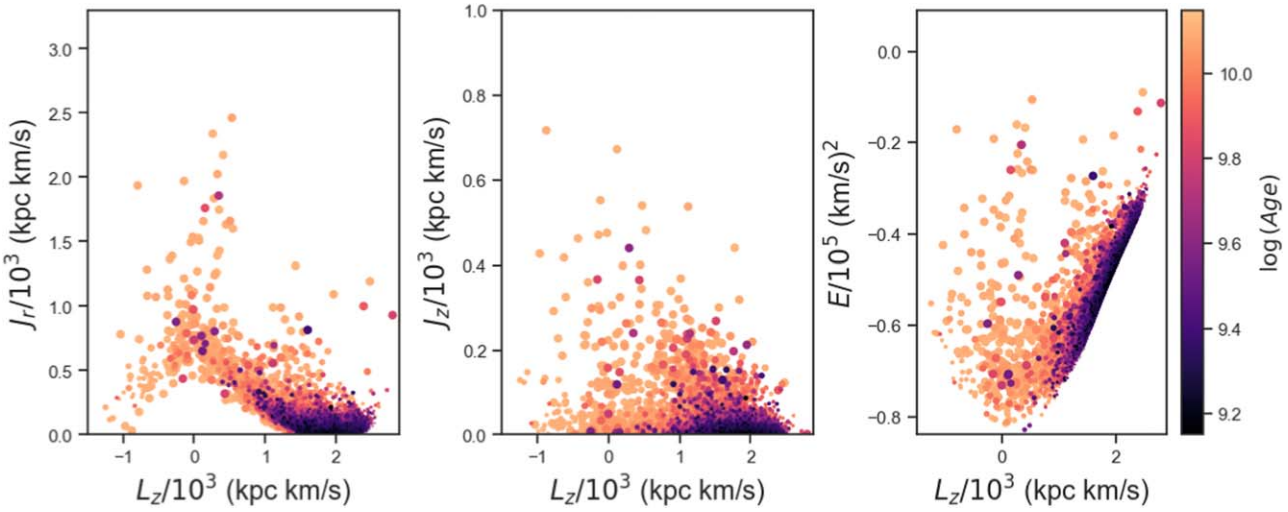

Figure 9. Older stars can be found in any populated region of dynamic phase space, but younger stars are virtually purely associated with cold disk kinematics. The dynamical distribution of our sample stars in action space (left two panels) and in terms of integrals of motion (right panel). The points are color coded by their derived age, and the size of the points is proportional to their isolation in J_r–J_z space.

The metal-poor annex totals 112,062 stars, of which 96,247 stars meet the photometric and blending criteria used for the main sample—that is, the distribution that we plot in the right panel of Figure 7. Of those, 14,670 stars have a derived age precision better than 7%, and 6768 have derived age precisions better than 5%.

Of the 96,247 metal-poor annex stars that meet our photometric and variability criteria, 10,015 have matches in LAMOST DR7, and we show their distribution in Figure 11. The two samples are consistent, with a median offset of 0.11 dex and a median absolute deviation of 0.10 dex. As with Figure 3, we do see a cloud of points for which the spectroscopic metallicities exceed the photometric metallicities. Here, we find that the error is due to specific failure modes of the photometric analysis. Some 30% of the stars in Figure 11 with derived metallicities satisfying $[\mathrm{Fe/H}] \leqslant -1.0$ have a difference in their photometric and spectroscopic metallicities exceeding 0.50 dex. For those, the mean derived ages are 24% lower, the mean derived extinctions are $\gtrsim 2\times$ greater, and the mean derived errors on the metallicities are $\gtrsim 5\times$ greater.

The most significant offset, however, is that due to whether or not there is an NUV measurement. For the 209 stars in Figure 11 with derived metallicities satisfying $[\mathrm{Fe/H}] \leqslant -1.0$ and which have an offset between the photometric and spectroscopic metallicity determinations exceeding $\Delta[\mathrm{Fe/H}] = 0.50$ dex, only one has an NUV measurement. In contrast, for the 486 other stars with derived metallicities satisfying $[\mathrm{Fe/H}] \leqslant -1.0$, 399 have NUV measurements. We conclude that NUV is simply more effective than u band at distinguishing metal-poor subgiant stars from young metal-rich turnoff stars with similar optical colors—particularly when the reddening is high.

The metal-poor annex yields significant potential for follow-up. Among the stars that satisfy our blending and variability criteria, have 7% precision in their age determinations, and which are brighter than $G = 14$, some 4649 have $[\mathrm{Fe/H}] \leqslant -1.00$, and some 3123 have $[\mathrm{Fe/H}] \leqslant -1.5$. Of these, roughly half are brighter than $G = 13$, further enabling follow-up study.

4.4.1. Metal-poor Annex Systematics and Uncertainties

We investigated the fidelity of our photospheric stellar parameters for the metal-poor annex by performing spectroscopic observations of apparently metal-poor subgiants (i.e., $[\mathrm{Fe/H}] \lesssim -1.0$), one young and one old. To remain as unbiased as possible, we selected stars observable at the time and from the place of observation based on their inferred metallicities and ages alone. We selected Gaia DR3 6032690864784481664 ($T_{\rm eff} = 6430 \pm 50$ K, $\log g = 3.90 \pm 0.02$, $[\mathrm{Fe/H}] = -1.13 \pm 0.13$, and $\tau = 6.3 \pm 0.4$ Gyr) and Gaia DR3 6310653893928413696 ($T_{\rm eff} = 6010 \pm 60$ K, $\log g = 4.02 \pm 0.02$, $[\mathrm{Fe/H}] = -0.82 \pm 0.08$, and $\tau = 11.2 \pm 0.8$ Gyr).

We collected their spectra with the Magellan Inamori Kyocera Echelle spectrograph on the Magellan Clay Telescope at Las Campanas Observatory (R. Bernstein et al. 2003; S. A. Shectman & M. Johns 2003). We used the 0.″7 slit with standard blue and red grating azimuths, yielding spectra between 335 and 950 nm with resolution $R \approx 40{,}000$ in the blue and $R \approx 31{,}000$ in the red arms. We collected all calibration data (e.g., bias, quartz and "milky" flat fields, and ThAr lamp frames) in the afternoon before each night of observations. We reduced the raw spectra and calibration frames using the `CarPy`[11] software package (D. D. Kelson et al. 2000; D. D. Kelson 2003; D. D. Kelson et al. 2014). We placed the spectra in the rest frame and continuum normalized them using Spectroscopy Made Harder (A. R. Casey 2014).[12]

We analyzed Gaia DR3 6032690864784481664 and Gaia DR3 3631065389392841369 6 using the methodology described in H. Reggiani et al. (2021, 2022a, 2022b, 2023, 2024). That methodology initially uses the classical excitation–ionization–reduced equivalent width balance approach to infer an initial set of photospheric stellar parameters. Those parameters are then included in the likelihood of an `isochrones` analysis that in all other details corresponds to the analyses described in Section 3. We next use ($T_{\rm eff}$, $\log g$) samples from the resulting `isochrones` posteriors as constraints on the spectroscopic analysis and recalculate [Fe/H] using reduced equivalent width balance. The photospheric stellar parameters are again included in an `isochrones` analysis. This procedure is iterated a few times until the photospheric stellar parameters have converged. Using this

[11] http://code.obs.carnegiescience.edu/mike
[12] https://github.com/andycasey/smhr/tree/py38-mpl313

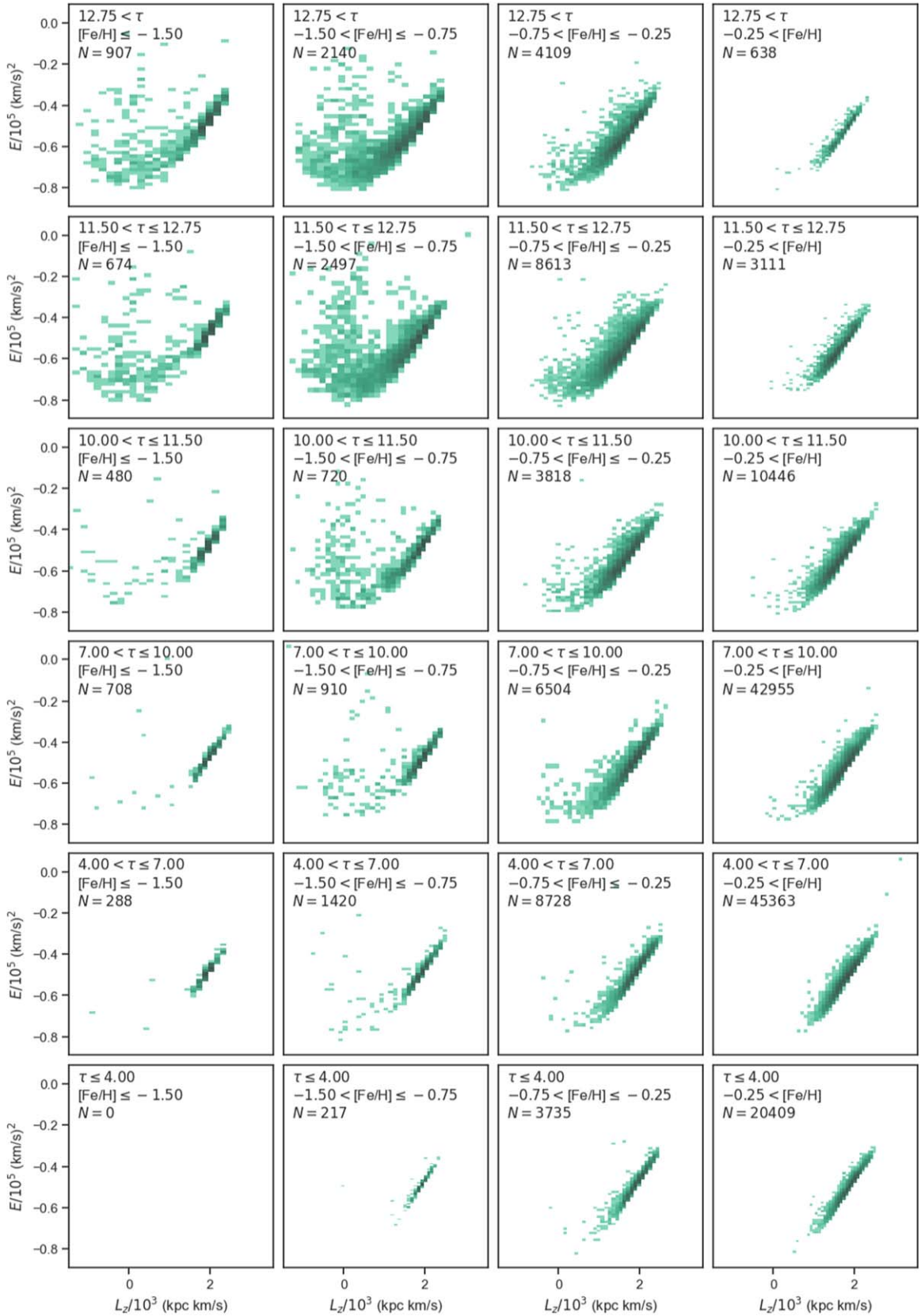

Figure 10. The derived E vs. L_Z distribution functions for the orbits of the stars in our combined primary + metal-poor annex sample, in six different bins of age (increasing upwards) and four different bins of metallicity (increasing to the right) for 24 total bins. We include 169,411 stars that satisfy our variability and blending criteria, for which the 1σ precision in the derived ages is better than 10%, and for which the 1σ precision in the derived [Fe/H] is better than 0.20 dex. Younger stars have nearly entirely disk-like kinematics, whereas older stars can be found in any region of kinematic phase space where there are stars to be found, including the disk.

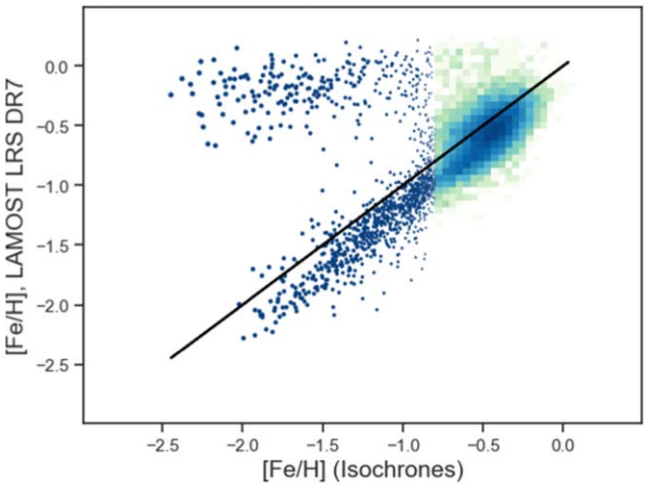

Figure 11. For stars in our metal-poor annex that have been observed by LAMOST. The cloud of stars for which the photometric metallicities are underestimated are largely a product of less reliable ultraviolet photometry and less certain reddening measurements. For the vast majority of stars, the astro-photometric metallicities are generally consistent with the spectroscopically derived metallicities

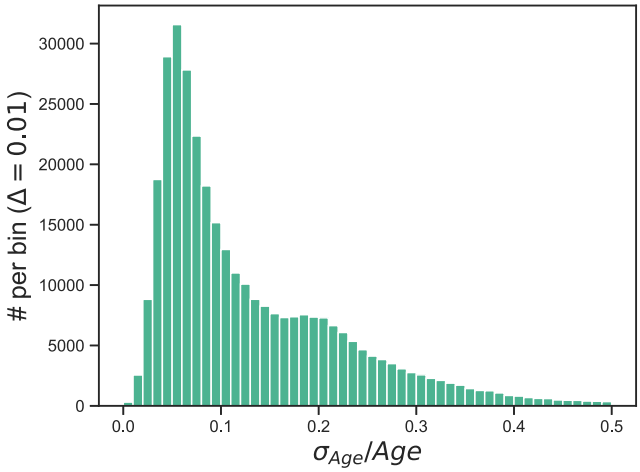

Figure 12. Distribution of the derived age precision for 335,778 stars in our combined primary sample and metal-poor annex that meet our quality inclusion criteria for variability and crossmatching between surveys. The median age precision is 9.5% and the mean age precision of 13.4%, with a long tail to higher errors.

approach, for Gaia DR3 6032690864784481664 we find $T_{\rm eff} = 6310 \pm 50$ K, $\log g = 3.99 \pm 0.02$, $[{\rm Fe/H}] = -0.44 \pm 0.10$, and $\tau = 4.8 \pm 0.3$ Gyr; for Gaia DR3 6310653893928413696 we find $T_{\rm eff} = 6030 \pm 10$ K, $\log g = 3.96 \pm 0.01$, $[{\rm Fe/H}] = -1.21 \pm 0.02$, and $\tau = 13.4 \pm 0.1$ Gyr.

While our spectroscopy-based metallicity inference for Gaia DR3 6032690864784481664 is much higher than the metallicity returned by our default analysis, the age inferences from both approaches agree that the star is mature. Likewise, the $T_{\rm eff}$ and $\log g$ inferences from both approaches agree to within 120 K and 0.1 dex. While our spectroscopy-based metallicity inference for Gaia DR3 6310653893928413696 is marginally lower than the metallicity returned by our default analysis, the $T_{\rm eff}$ and $\log g$ values are in excellent agreement. Both our default and spectroscopic analyses agree that Gaia DR3 6310653893928413696 is ancient.

As we argued above, GALEX data are a necessary ingredient for our highest-quality stellar parameter inferences. GALEX data are unavailable for both Gaia DR3 6032690864784481664 and Gaia DR3 6310653893928413696 though, so the spectroscopic results presented here represent a worst-case scenario for the accuracy of our metal-poor stellar parameter inferences. Gaia DR3 6032690864784481664 has $T_{\rm eff} \approx 6400$ K placing it at the warm end of our subgiant $T_{\rm eff}$ distribution, so it seems that GALEX photometry is especially important for accurate metallicity inferences for relatively warm subgiants.

4.5. On the Uncertainties in the Derived Ages

As delineated in Equation (1) and can be inferred from Figure 1, a 1% precision in the parallaxes should correspond to a 2% precision in the derived ages in the best-case scenario where the stellar temperature and metallicity are precisely determined. It thus needs to be better understood why, in spite of a median parallax precision of $\pi/\sigma_\pi = 80$, we achieve, for the 335,778 stars in our combined primary sample and metal-poor annex that meet our quality inclusion criteria, a median age precision of 9.5% and a mean age precision of 13.4% (distribution shown in Figure 12). We note that these values drop to 8.4% and 12.7%, respectively, for stars with GALEX photometry, indicative of the greater diagnostic power of space-based, ultraviolet photometry.

Here we discuss two factors that are exacerbating the uncertainties in the derived ages, and their prospects for improvement.

The first factor is the degeneracy between the uncertainties in metallicity and age. The average correlation coefficient between the uncertainties in log(age) and [Fe/H] is −0.72. Thus, the error in metallicity, which can be largely attributed to uncertainties in the ultraviolet photometry and in the 3D extinction maps, is responsible for most of the error in the derived ages. This problem will be mitigated in the near future as the availability of robust ultraviolet photometry is expected to both increase and improve.

To further explore the origin of the uncertainties in the derived ages, we define a coarse estimate of the uncertainty in apparent distance modulus σ_μ, as follows:

$$\sigma_\mu^2 = \left(\frac{5}{\ln 10}\frac{\sigma_\pi}{\pi}\right)^2 + \sigma_{AV}^2. \quad (5)$$

In the middle panel of Figure 13, we show that the derived ages are indeed more precise for stars with smaller values of σ_μ, but that another significant contributor to the uncertainty in derived ages is that of the derived EEP of the star. That is because our selection function inevitably includes not only subgiant branch stars, but also main-sequence turnoff and first-ascent red giant branch stars, as shown in the left panel. Returning to the middle panel, we see that we do achieve excellent precision in the derived ages for stars with EEP values of around 460, corresponding to subgiant branch stars. The errors are much higher for those stars which are either turnoff stars (EEP ≈ 420) or first-ascent red giant branch stars (EEP $\gtrapprox 475$). In our case, some 75% of the stars in our sample have derived EEPs in the range ($450 \leqslant {\rm EEP} \leqslant 475$) approximately corresponding to the subgiant branch. On the left panel, we show that the normalized distribution of the derived ages for the subgiant stars, as approximated by those stars with ($450 \leqslant {\rm EEP} \leqslant 475$), has a mode at around 5%. A selection function that is more tightly focused on these stars could likely be constructed by making a finer use of ultraviolet photometry,

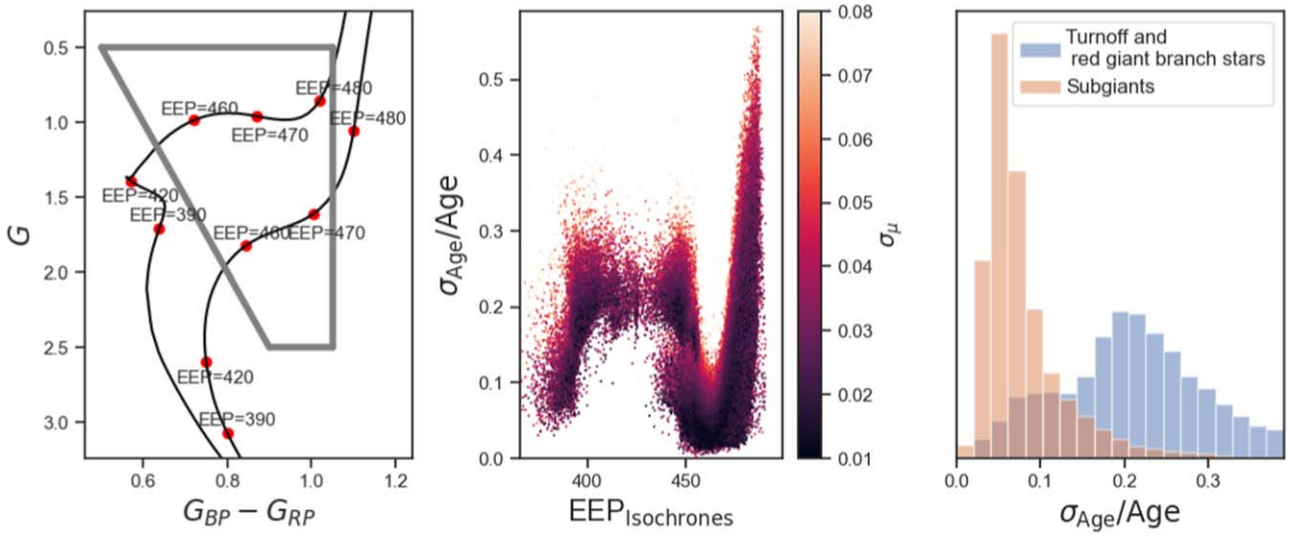

Figure 13. Left: MIST isochrones of solar metallicity and of ages $\tau = 3$ and 8 Gyr, with indicative EEPs shown as red points. Middle: the uncertainty in the derived ages as a function of EEP, color coded by the uncertainty in the apparent distance modulus. Right: Normalized distribution of the age precisions for stars with $450 \leqslant \mathrm{EEP} \leqslant 475$ (subgiants, orange) and other stars (blue). We see that the derived ages are more precise at all phases of stellar evolution when the assumed apparent distance moduli are more precise, and the best precision is achieved on the subgiant branch.

and to make the color–magnitude selection box more metallicity dependent.

5. Summary, Discussion, and Conclusion

In this investigation, we have demonstrated that the combination of available data for parallaxes, ultraviolet through infrared photometry, variability, and three-dimensional extinction maps are adequate to obtain precise ages and metallicities for nearly half a million subgiant stars. This is, among other successes, an indicator of the spectacular triumph within astronomy of each of improving observations and related technology, increasingly sophisticated computational and data analysis methods, and improving stellar evolution models. Our metal-poor annex is also, arguably, among the largest samples available for detailed investigative and spectroscopic follow-up of the earliest phases of Milky Way formation and assembly. Below, we discuss some of the larger sources of uncertainty in our results, and prospects for improved analysis in the future,

5.1. Major Systematic Uncertainties: Variability, Elemental Abundance Variations, and Bolometric Corrections

Undiagnosed binaries, products of binary evolution, and other variables are plausibly the most significant source of systematic error in our sample. As can be seen in Figure 4, our methods identify some, but not all, such stars on the subgiant branches of the open clusters M67 and NGC 188. This may be an overrepresentation of this error source, as these clusters are both more distant than the majority of our sample, and so the binary diagnostic criteria may be less reliable. The issue may also mitigate over time—we are eager to find out how many additional variables will be identified once Gaia Data Release 4 (DR4) is released, as the astrometric and photometric time series will cover 66 rather than 34 months of data, and individual radial velocity measurements will become available.

A second systematic uncertainty is that our analysis has assumed the scaled solar composition isochrones available from the MIST database. We have done so as these are the stellar models used by the `isochrones` package. The most obvious uncertainty here is that the assumption of scaled solar composition is not valid for stars of the thick disk, halo, and many accreted streams (and thus the most metal-poor stars), as these stars tend to be enhanced in the α-elements (O, Ne, Mg, Si, S, Ar, Ca, and Ti; see, e.g., C. Sneden et al. 1991; A. McWilliam & R. M. Rich 1994; A. Alves-Brito et al. 2010; T. Bensby et al. 2014; M. R. Hayden et al. 2015), and often also have variations in carbon and nitrogen abundances (T. Masseron & G. Gilmore 2015; D. Horta et al. 2021), and possibly helium (L. Casagrande et al. 2007; M. Gennaro et al. 2010). These abundance changes will effect the evolutionary state, temperature, luminosity, and intrinsic colors of stars of otherwise identical mass and age. This is an issue that should resolve itself in the future, as the next generation of MIST isochrones will include stellar models of variable α-abundance (A. Dotter, private communication).

5.2. Major Quantitative Limitation: The Availability of Ultraviolet through Infrared Photometry for Stars with Precise Parallaxes

Our optical, Gaia-based selection query for candidate subgiant stars in our primary sample, which is shown graphically in Figure 1 and for which we provide the ADQL query in the Appendix, yields 1,998,909 sources. Once we require unambiguous matches between Gaia DR2 and Gaia DR3 and full photometry from 2MASS and WISE, we are left with 1,661,347 matches. Once we require reddening data, and correct the color–magnitude selection box in Figure 1 to be based on estimated values of $(G_{\mathrm{BP}} - G_{\mathrm{BP}})_0$, we are left with a sample of 618,598 stars. Once we then require $A_V \leqslant 0.50$, the sample drops to 462,045 stars. Once we also require an ultraviolet photometric measurement, the sample drops to 289,718 stars.

These numbers will be shifted upwards by a significant amount with future data. For example, Gaia DR4 and Gaia Data Release 5 will, respectively, cover an expected 66 and 120 months of data, resulting in parallaxes that are respectively 2 and 4 times more precise than those of Gaia DR3. We should eventually be able to sample stars at distances that are up to 4

times further away, enabling the initial sample to exceed 10^7 subgiant stars. At the ultraviolet end, vastly more data will be available in the future by missions such as ULTRASAT (Y. Shvartzvald et al. 2024), UVEX (S. R. Kulkarni et al. 2021), and the Vera Rubin Observatory (Ž. Ivezić et al. 2019). The first two will provide in measurements in two bands similar to those of GALEX but down to 23rd and 25th magnitudes, respectively, and the third will provide *u*-band photometry for three quarters of the sky down to 26th magnitude. For each of these, it is expected that the PSF will be sharper and that the absolute flux calibration will be more accurate than currently available ultraviolet data. At the near-infrared end, large parts of the sky will be observed to 10 or more magnitudes deeper than 2MASS, and with a 5–10× smaller PSF, by Euclid (R. Laureijs et al. 2011) and the Nancy Grace Roman Space Telescope (D. Spergel et al. 2015).

5.3. Major Improvements Feasible with Currently Available Data

Our aim with this project was both to develop a catalog and to develop a methodology. Thus, our use of publicly available data was extensive, but it was not exhaustive.

Four large photometric surveys that we did not make use are the Southern Photometric Local Universe Survey (C. Mendes de Oliveira et al. 2019), the VST Photometric Hα Survey of the Southern Galactic Plane and Bulge (J. E. Drew et al. 2014), The Blanco DECam Bulge Survey (C. I. Johnson et al. 2020), and the DeCam Plane Survey (E. F. Schlafly et al. 2018). The first three have ultraviolet and optical photometry for large parts of the sky down to approximately 20th magnitude, and the fourth has optical *grizY* photometry for approximately two billion point sources across the Galactic plane. These data sets would undoubtedly significantly increase our sample size, and are obvious candidates for inclusion in any follow-up study.

Another option with the possibility of qualitatively enhancing the analysis in this work is the inclusion of the spectra from Gaia, specifically the BP/RP spectra (J. M. Carrasco et al. 2021) and that from the radial velocity spectrometer (RVS; D. Katz et al. 2019). The former cover the wavelength range 300–10500 Å with a resolution between 13 and 85, and the latter cover the wavelength range 8450–8720 Å with a resolution of 11,500.

In our Figure 3, we show that metallicity measurements from the RVS are reliable down to $[\mathrm{Fe/H}] \approx -0.50$, and this was also shown to be the case for the BP/RP spectra by C. E. C. Witten et al. (2022), see their Figure 4. However, in both cases the limitations of these spectra, likely due to a degeneracy between metallicity and temperature in the regime of weaker absorption lines, have been quantified when the spectra are used to determine stellar parameters on their own. The diagnostic power would undoubtedly be greatly enhanced once one includes information from parallaxes, precise photometry in the ultraviolet and infrared, and constraints from published three-dimensional extinction maps.

5.4. Conclusions

This study of astro-photometric age and metallicity determinations for solar neighborhood subgiant stars represents one of the largest catalogs of stars with precisely measured relative ages, for which the distribution is shown in our Figure 7.

We have validated our analysis using several different independent and complementary methods. We showed, via comparisons with open clusters, that we can infer precise relative ages; and we showed, via our comparison to large spectroscopic surveys (APOGEE, GALAH, and LAMOST) that we can infer consistently accurate metallicities across the interval $-2.0 \leqslant [\mathrm{Fe/H}] \leqslant +0.50$ to a precision no worse than ∼0.10 dex, and which include the effect of systematics such as undiagnosed binaries. We have also shown that the median systematic error in the bolometric zero-points is approximately 0.01 mag, and that our analysis is insensitive to small changes in the input data and priors.

Our dynamical analysis, shown in Figures 9 and 10, shows that older stars are to be found in any region of dynamic phase space where there are stars of any age to be found, but that younger stars are progressively more constrained to colder regions of dynamic phase space. The range of values of J_r and J_z drops to being closer and closer to zero as the ages drop, and the orbits become more tightly constrained to circular orbits as per their distributions in the integrals of motion E and L_z.

Our metal-poor annex is one of the largest catalogs of metal-poor stars with precise metallicities and ages—it includes over 4500 stars with both $[\mathrm{Fe/H}] \leqslant -1.00$, age precisions better than 7%, and that are brighter than $G = 14$. Of those, 3123 stars have best-fit metallicities satisfying $[\mathrm{Fe/H}] \leqslant -1.50$.

We look forward to further vetting of this method by subsequent studies, as well as the promising prospects to see the sample sizes increase as future data become available, and for the precision to improve as more data are included.

Acknowledgments

We thank Tim Morton, Rosemary Wyse, Luca Casagrande, Sven Buder, and Aaron Dotter for helpful discussions. D.M.N. acknowledges support from NASA under award Number 80NSSC21K1570 and award Number 80NSSC19K058. H.R. acknowledges support from a Carnegie Fellowship. This research made use of Astropy,[13] a community-developed core Python package for Astronomy, (Astropy Collaboration et al. 2013; A. M. Price-Whelan et al. 2018). This research has made use of the WEBDA database, operated at the Department of Theoretical Physics and Astrophysics of the Masaryk University This work has made use of data from the European Space Agency (ESA) mission Gaia (https://www.cosmos.esa.int/gaia), processed by the Gaia Data Processing and Analysis Consortium (DPAC; https://www.cosmos.esa.int/web/gaia/dpac/consortium). Funding for the DPAC has been provided by national institutions, in particular the institutions participating in the Gaia Multilateral Agreement. The national facility capability for SkyMapper has been funded through ARC LIEF grant LE130100104 from the Australian Research Council, awarded to the University of Sydney, the Australian National University, Swinburne University of Technology, the University of Queensland, the University of Western Australia, the University of Melbourne, Curtin University of Technology, Monash University, and the Australian Astronomical Observatory. SkyMapper is owned and operated by The Australian National University's Research School of Astronomy and Astrophysics. The survey data were processed and provided by the SkyMapper Team at ANU. The SkyMapper node of the

[13] http://www.astropy.org

All-Sky Virtual Observatory (ASVO) is hosted at the National Computational Infrastructure (NCI). Development and support of the SkyMapper node of the ASVO has been funded in part by Astronomy Australia Limited (AAL), the Australian Government through the Commonwealth's Education Investment Fund (EIF), and National Collaborative Research Infrastructure Strategy (NCRIS), particularly the National eResearch Collaboration Tools and Resources (NeCTAR) and the Australian National Data Service Projects (ANDS). This publication makes use of data products from the Two Micron All Sky Survey, which is a joint project of the University of Massachusetts and the Infrared Processing and Analysis Center/California Institute of Technology, funded by the National Aeronautics and Space Administration and the National Science Foundation. This publication makes use of data products from the Wide-field Infrared Survey Explorer, which is a joint project of the University of California, Los Angeles, and the Jet Propulsion Laboratory/California Institute of Technology, funded by the National Aeronautics and Space Administration. Funding for the Sloan Digital Sky Survey IV has been provided by the Alfred P. Sloan Foundation, the U.S. Department of Energy Office of Science, and the Participating Institutions. SDSS-IV acknowledges support and resources from the Center for High-Performance Computing at the University of Utah. The SDSS website is www.sdss.org. SDSS-IV is managed by the Astrophysical Research Consortium for the Participating Institutions of the SDSS Collaboration including the Brazilian Participation Group, the Carnegie Institution for Science, Carnegie Mellon University, the Chilean Participation Group, the French Participation Group, Harvard-Smithsonian Center for Astrophysics, Instituto de Astrofísica de Canarias, The Johns Hopkins University, Kavli Institute for the Physics and Mathematics of the Universe (IPMU)/University of Tokyo, the Korean Participation Group, Lawrence Berkeley National Laboratory, Leibniz Institut fúr Astrophysik Potsdam (AIP), Max-Planck-Institut fúr Astronomie (MPIA Heidelberg), Max-Planck-Institut fúr Astrophysik (MPA Garching), Max-Planck-Institut fúr Extraterrestrische Physik (MPE), National Astronomical Observatories of China, New Mexico State University, New York University, University of Notre Dame, Observatário Nacional/MCTI, The Ohio State University, Pennsylvania State University, Shanghai Astronomical Observatory, United Kingdom Participation Group, Universidad Nacional Autónoma de México, University of Arizona, University of Colorado Boulder, University of Oxford, University of Portsmouth, University of Utah, University of Virginia, University of Washington, University of Wisconsin, Vanderbilt University, and Yale University.

Software: Astropy (Astropy Collaboration et al. 2013; A. M. Price-Whelan et al. 2018), SciPy (E. Jones et al. 2001; P. Virtanen et al. 2020), NumPy (T. Oliphant 2006), isochrones (T. D. Morton 2015), Multinest (F. Feroz & M. P. Hobson 2008; F. Feroz et al. 2009, 2019), pandas (W. McKinney 2010), scipy (P. Virtanen et al. 2020), Matplotlib (J. D. Hunter 2007), and TOPCAT (M. B. Taylor 2005)

Appendix A
Photometric Data Catalog Construction and Quality Flags

We aim to select data which are relatively robust, by making use of the data quality flags suggested by the collaborations responsible for each data set, which are restated below.

1. From the Gaia data archive,[14] we select numerous measurements, including some that are ultimately not used. The most significant measurements that we select are the DR3 astrometric measurements, the DR2 mean photometric measurements and the SkyMapper DR2, SDSS DR13, 2MASS PSC, and WISE AllWISE crossmatches identified by the Gaia collaboration. Here, we show the full query that can be used to download a parent sample to our main sample; the color–magnitude selection box for the metal-poor annex is adjusted in the manner described in Section 2. When we last ran the query on 2023 March 1, it took the Gaia server 4269 s to complete, for which we got 1,998,909 matches. We then removed 902 sources for which there were multiple Gaia DR2 sources per Gaia DR3 source. As this query may take longer to compute in periods of heavy user use, we recommend splitting it into subqueries in R.A.

```
SELECT gaiadr3.source_id AS dr3_source_id,
e.original_ext_source_id AS skymapper_id,
f.original_ext_source_id AS sdss_id,
g.original_ext_source_id AS twomass_id,
h.original_ext_source_id AS allwise_id,
i.original_ext_source_id AS panstarrs1_id,
b.dr2_source_id AS dr2_source_id,
gaiadr2.phot_g_mean_mag AS dr2_gmag,
gaiadr2.phot_bp_mean_mag AS dr2_bpmag,
gaiadr2.phot_rp_mean_mag AS dr2_rpmag,
gaiadr2.phot_bp_mean_flux_over_error as dr2_phot_bp_mean_flux_over_error,
gaiadr2.phot_g_mean_flux_over_error as dr2_phot_g_mean_flux_over_error,
gaiadr2.phot_rp_mean_flux_over_error as dr2_phot_rp_mean_flux_over_error,
gaiadr3.solution_id,
gaiadr3.random_index,
COORD1(EPOCH_PROP_POS(gaiadr3.ra, gaiadr3.dec, gaiadr3.parallax, gaiadr3.pmra,
```

[14] http://gea.esac.esa.int/archive/

(Continued)

```
gaiadr3.pmdec, gaiadr3.radial_velocity, gaiadr3.ref_epoch,2000)) AS ra2000,
COORD2(EPOCH_PROP_POS(gaiadr3.ra, gaiadr3.dec, gaiadr3.parallax, gaiadr3.pmra,
gaiadr3.pmdec, gaiadr3.radial_velocity, gaiadr3.ref_epoch,2000)) AS dec2000,
gaiadr3.ref_epoch,
gaiadr3.ra,
gaiadr3.dec,
gaiadr3.parallax,
gaiadr3.parallax_error,
gaiadr3.parallax_over_error,
gaiadr3.pmra,
gaiadr3.pmra_error,
gaiadr3.pmdec,
gaiadr3.pmdec_error,
gaiadr3.phot_g_n_obs,
gaiadr3.phot_g_mean_flux,
gaiadr3.phot_g_mean_flux_error,
gaiadr3.phot_g_mean_flux_over_error,
gaiadr3.phot_g_mean_mag,
gaiadr3.phot_bp_mean_mag,
gaiadr3.phot_rp_mean_mag,
gaiadr3.phot_bp_mean_flux_over_error,
gaiadr3.phot_rp_mean_flux_over_error,
gaiadr3.phot_variable_flag,
gaiadr3.l,
gaiadr3.b,
gaiadr3.astrometric_excess_noise_sig,
gaiadr3.visibility_periods_used,
gaiadr3.ruwe,
gaiadr3.astrometric_params_solved,
gaiadr3.ipd_gof_harmonic_amplitude,
gaiadr3.phot_bp_mean_flux_over_error,
gaiadr3.phot_rp_mean_flux_over_error,
gaiadr3.nu_eff_used_in_astrometry,
gaiadr3.pseudocolour,
gaiadr3.ecl_lat,
gaiadr3.radial_velocity,
gaiadr3.radial_velocity_error,
gaiadr3.grvs_mag,
gaiadr3.grvs_mag_error,
gaiadr3.rvs_spec_sig_to_noise,
d.r_lo_geo, d.r_med_geo, d.r_hi_geo,
j.teff_gspphot, j.logg_gspphot, j.mh_gspphot,
j.teff_gspspec, j.logg_gspspec, j.mh_gspspec, j.alphafe_gspspec, j.fem_gspspec,
j.mh_gspspec_lower,
j.mh_gspspec_upper,
j.flags_gspspec
FROM gaiadr3.gaia_source as gaiadr3
LEFT OUTER JOIN gaiadr3.dr2_neighbourhood b ON gaiadr3.source_id=b.dr3_source_id
LEFT OUTER JOIN gaiadr2.gaia_source gaiadr2 ON b.dr2_source_id=gaiadr2.source_id
LEFT OUTER JOIN external.gaiaedr3_distance d ON gaiadr3.source_id=d.source_id
LEFT OUTER JOIN gaiaedr3.skymapperdr2_best_neighbour e ON gaiadr3.source_id=e.source_id
LEFT OUTER JOIN gaiaedr3.sdssdr13_best_neighbour f ON gaiadr3.source_id=f.source_id
LEFT OUTER JOIN gaiaedr3.tmass_psc_xsc_best_neighbour g ON gaiadr3.source_id=g.source_id
LEFT OUTER JOIN gaiaedr3.allwise_best_neighbour h ON gaiadr3.source_id=h.source_id
LEFT OUTER JOIN gaiadr3.panstarrs1_best_neighbour i ON gaiadr3.source_id=i.source_id
LEFT OUTER JOIN gaiadr3.astrophysical_parameters j on gaiadr3.source_id=j.source_id
WHERE gaiadr3.phot_g_mean_mag-1.90*(gaiadr3.bp_rp) - 5*LOG10(d.r_med_geo) + 5 <=2.5
AND gaiadr3.phot_g_mean_mag-1.90*(gaiadr3.bp_rp) - 5*LOG10(d.r_med_geo) + 5 >=0.50
AND gaiadr3.phot_g_mean_mag-1.90*(gaiadr3.bp_rp) - 5*LOG10(d.r_med_geo) + 5 <=
5*(gaiadr3.bp_rp-0.90)+2.5
AND gaiadr3.bp_rp <=1.30
AND gaiadr3.duplicated_source='FALSE'
AND gaiadr3.phot_proc_mode=0
AND gaiadr3.phot_variable_flag !='VARIABLE'
```

(Continued)

```
AND gaiadr3.non_single_star=0
AND gaiadr3.ruwe < =1.4
AND gaiadr3.parallax_over_error >=50
AND gaiadr3.ipd_gof_harmonic_amplitude < =0.10
AND gaiadr3.astrometric_params_solved=31
AND abs(gaiadr2.phot_g_mean_mag-gaiadr3.phot_g_mean_mag) < =0.20
```

2. Corrected zero-points to the Gaia DR3 parallaxes are applied using the prescription of L. Lindegren et al. (2021), with the source code downloaded from https://gitlab.com/icc-ub/public/gaiadr3_zeropoint.
3. GALEX FUV and NUV photometry and associated uncertainties data are downloaded from the Revised Catalog of GALEX Ultraviolet Sources (L. Bianchi et al. 2017). We require that the centroid of the GALEX source be within 2.″5 of the centroid of the Gaia DR3 source, where we use the J2000 coordinates of the latter for the comparison. We use the FUV photometry if the parameter FUV_artifact (called Fafl in the Vizier table) does not have bits 2 or 3, and similarly for NUV photometry and the parameter NUV_artifact (called Nafl in the Vizier table). To avoid contamination from ultraviolet-bright sources that are not the intended stars, we require that the FUV and NUV match be the same, and that $(\mathrm{FUV}-\mathrm{NUV})\geqslant 3.75$.
4. Skymapper *uvgriz* photometry and associated uncertainties (C. A. Onken et al. 2019), for sources as delineated by the Skymapper identifiers from the Gaia archive are downloaded from the dr2.master table, which is accessible from the ESO Gaia archive at https://gea.esac.esa.int/archive/ using the following query:

   ```
   SELECT a.object_id, a.u_flags, a.u_nimaflags, a.u_ngood, a.u_psf, a.e_u_psf, a.v_flags, a.v_nimaflags, a.v_ngood, a.v_psf, a.e_v_psf, a.g_flags, a.g_nimaflags, a.g_ngood, a.g_psf, a.e_g_psf, a.r_flags, a.r_nimaflags, a.r_ngood, a.r_psf, a.e_r_psf, a.i_flags, a.i_nimaflags, a.i_ngood, a.i_psf, a.e_i_psf, a.z_flags, a.z_nimaflags, a.z_ngood, a.z_psf, a.e_z_psf FROM external.skymapperdr2_master AS a INNER JOIN user_ID.InputTable AS b ON a.object_id=b.skymapper_id
   ```

   For each bandpass "x," we require (x_flags = 0), (x_nimaflags= 0), and (x_ngood > =1). We also require $|G-g_{\mathrm{sm}}+0.35|\leqslant 0.30$, to reduce the number of spurious matches. The Skymapper data are described at http://skymapper.anu.edu.au/data-release/.
5. SDSS *ugriz* photometry and associated uncertainties (R. Ahumada et al. 2020), for sources as delineated by the SDSS identifiers from the Gaia archive, are downloaded using CASJobs at http://skyserver.sdss.org/casjobs/ using the query described below. We also require $|G-g_{\mathrm{SDSS}}+0.55|\leqslant 0.40$, to reduce the number of spurious matches.

```
SELECT S.objID,
CASE WHEN ((S.flags_u & 0x10000000) !=0) AND ((S.flags_u & 0x8100000c00a4)=0) AND (((S.flags_u & 0x4000000000000)
  =0) or (S.psfmagerr_u < =0.2)) AND (((S.flags_u & 0x100000000000)=0) or (S.flags_u & 0x1000)=0) THEN S.
  psfMag_u ELSE null END AS psfMag_u,
CASE WHEN ((S.flags_u & 0x10000000) !=0) AND ((S.flags_u & 0x8100000c00a4)=0) AND (((S.flags_u & 0x4000000000000)
  =0) or (S.psfmagerr_u < =0.2)) AND (((S.flags_u & 0x100000000000)=0) or (S.flags_u & 0x1000)=0) THEN S.
  psfMagErr_u ELSE null END AS psfMagErr_u,
CASE WHEN ((S.flags_g & 0x10000000) !=0) AND ((S.flags_g & 0x8100000c00a4)=0) AND (((S.flags_g & 0x4000000000000)
  =0) or (S.psfmagerr_g < =0.2)) AND (((S.flags_g & 0x100000000000)=0) or (S.flags_g & 0x1000)=0) THEN S.
  psfMag_g ELSE null END AS psfMag_g,
CASE WHEN ((S.flags_g & 0x10000000) !=0) AND ((S.flags_g & 0x8100000c00a4)=0) AND (((S.flags_g & 0x4000000000000)
  =0) or (S.psfmagerr_g < =0.2)) AND (((S.flags_g & 0x100000000000)=0) or (S.flags_g & 0x1000)=0) THEN S.
  psfMagErr_g ELSE null END AS psfMagErr_g,
CASE WHEN ((S.flags_r & 0x10000000) !=0) AND ((S.flags_r & 0x8100000c00a4)=0) AND (((S.flags_r & 0x4000000000000)
  =0) or (S.psfmagerr_r < =0.2)) AND (((S.flags_r & 0x100000000000)=0) or (S.flags_r & 0x1000)=0) THEN S.
  psfMag_r ELSE null END AS psfMag_r,
CASE WHEN ((S.flags_r & 0x10000000) !=0) AND ((S.flags_r & 0x8100000c00a4)=0) AND (((S.flags_r & 0x4000000000000)
  =0) or (S.psfmagerr_r < =0.2)) AND (((S.flags_r & 0x100000000000)=0) or (S.flags_r & 0x1000)=0) THEN S.
  psfMagErr_r ELSE null END AS psfMagErr_r,
CASE WHEN ((S.flags_i & 0x10000000) !=0) AND ((S.flags_i & 0x8100000c00a4)=0) AND (((S.flags_i & 0x4000000000000)
  =0) or (S.psfmagerr_i < =0.2)) AND (((S.flags_i & 0x100000000000)=0) or (S.flags_i & 0x1000)=0) THEN S.
  psfMag_i ELSE null END AS psfMag_i,
CASE WHEN ((S.flags_i & 0x10000000) !=0) AND ((S.flags_i & 0x8100000c00a4)=0) AND (((S.flags_i & 0x4000000000000)
  =0) or (S.psfmagerr_i < =0.2)) AND (((S.flags_i & 0x100000000000)=0) or (S.flags_i & 0x1000)=0) THEN S.
  psfMagErr_i ELSE null END AS psfMagErr_i,
```

(Continued)

```
CASE WHEN ((S.flags_z & 0x10000000) !=0) AND ((S.flags_z & 0x8100000c00a4)=0) AND (((S.flags_z & 0x400000000000)
  =0) or (S.psfmagerr_z <=0.2)) AND (((S.flags_z & 0x100000000000)=0) or (S.flags_z & 0x1000)=0) THEN S.
  psfMag_z ELSE null END AS psfMag_z,
CASE WHEN ((S.flags_z & 0x10000000) !=0) AND ((S.flags_z & 0x8100000c00a4)=0) AND (((S.flags_z & 0x400000000000)
  =0) or (S.psfmagerr_z <=0.2)) AND (((S.flags_z & 0x100000000000)=0) or (S.flags_z & 0x1000)=0) THEN S.
  psfMagErr_z ELSE null END AS psfMagErr_z
INTO mydb.OutputFile FROM Star as S
INNER JOIN MyDB.InputFile AS c ON S.objID=c.sdss_id
```

6. PS1 *grizY* photometry and associated uncertainties (J. L. Tonry et al. 2012; H. A. Flewelling et al. 2020), for sources as delineated by the PS1 identifiers from the Gaia archive, are downloaded using CASJobs at https://mastweb.stsci.edu/ps1casjobs/default.aspx using the following query described below. Here, the values 14.5, 15.0, 15.0, 14.0, and 13.0 represent thresholds that we use as precautions against saturation artifacts. We also require $|G - g_{\rm PS} + 0.50| \leqslant 0.30$, to reduce the number of spurious matches.

```
SELECT a.objID,
CASE WHEN ((a.gQfPerfect > 0.85) AND (a.gMeanPSFMag > 14.5)) THEN a.gMeanPSFMag ELSE null END AS gMeanPSFMag,
CASE WHEN ((a.gQfPerfect > 0.85) AND (a.gMeanPSFMag > 14.5)) THEN a.gMeanPSFMagErr ELSE null END AS gMeanPSFMagErr,
CASE WHEN ((a.rQfPerfect > 0.85) AND (a.rMeanPSFMag > 15.0)) THEN a.rMeanPSFMag ELSE null END AS rMeanPSFMag,
CASE WHEN ((a.rQfPerfect > 0.85) AND (a.rMeanPSFMag > 15.0)) THEN a.rMeanPSFMagErr ELSE null END AS rMeanPSFMagErr,
CASE WHEN ((a.iQfPerfect > 0.85) AND (a.iMeanPSFMag > 15.0)) THEN a.iMeanPSFMag ELSE null END AS iMeanPSFMag,
CASE WHEN ((a.iQfPerfect > 0.85) AND (a.iMeanPSFMag > 15.0)) THEN a.iMeanPSFMagErr ELSE null END AS iMeanPSFMagErr,
CASE WHEN ((a.zQfPerfect > 0.85) AND (a.zMeanPSFMag > 14.0)) THEN a.zMeanPSFMag ELSE null END AS zMeanPSFMag,
CASE WHEN ((a.zQfPerfect > 0.85) AND (a.zMeanPSFMag > 14.0)) THEN a.zMeanPSFMagErr ELSE null END AS zMeanPSFMagErr,
CASE WHEN ((a.yQfPerfect > 0.85) AND (a.yMeanPSFMag > 13.0)) THEN a.yMeanPSFMag ELSE null END AS yMeanPSFMag,
CASE WHEN ((a.yQfPerfect > 0.85) AND (a.yMeanPSFMag > 13.0)) THEN a.yMeanPSFMagErr ELSE null END AS yMeanPSFMagErr
INTO mydb.OutputFile
FROM PanSTARRS_DR2.MeanObjectView AS a
INNER JOIN MyDB.InputFile AS b ON a.objid=b.panstarrs1_id
INNER JOIN (
SELECT DISTINCT d.objid
FROM PanSTARRS_DR2.StackObjectAttributes AS d
INNER JOIN MyDB.InputFile AS e ON d.objid=e.panstarrs1_id
WHERE d.primaryDetection > 0
) c ON a.objid=c.objid
WHERE a.nDetections > 5
AND (a.rMeanPSFMag-a.rMeanKronMag < 0.05)
```

7. 2MASS *JHK*$_s$ photometry and associated uncertainties (M. F. Skrutskie et al. 2006) are downloaded from the NASA/IPAC Infrared Science Archive at https://irsa.ipac.caltech.edu/frontpage/. For each source, we require `use_src = 1`, for each band we require `(ph_qual = "A") or (rd_flg = {"1","3"})`, and we require a 1″ match between the 2MASS astrometry and that from the R.A. (J2000) and decl. (J2000) astrometry computed from Gaia DR3 astrometry.
8. WISE W_1W_2 photometry and associated uncertainties (E. L. Wright et al. 2010) are downloaded from the NASA/IPAC Infrared Science Archive. For brighter sources ($8 \geqslant W_1 \geqslant 2$, $7 \geqslant W_2 \geqslant 1.5$) we use the WISE All-Sky photometric catalog, whereas for fainter ($W_1 \geqslant 8$, $W_2 \geqslant 7$) sources we use the AllWISE catalog. For each bandpass, we require `(ph_qual = {"A","B"})`, `(ext_flag = 0)`, and `cc_flags = {"0","d","p","h","o"}`. We also download the W_3 and W_4 photometry and associated uncertainties, but they do not contribute to our analysis.

Appendix B
Spectroscopic Comparison Data Catalog Construction and Quality Flags

1. Gaia spectroscopic parameters from the high-resolution channel are downloaded from the Gaia data archive, specifically from the `gaiadr3.astrophysical_parameters` catalog. For the parameter `flags_gspspec`, which has an injective mapping onto `gaiadr3.source_id`, we require that the first six parameters of the string be equal to "0," the seventh character be one of {"0," "1"}, and the eighth, eleventh, and twelfth characters be equal to "0." There are no constraints on the remaining characters.
2. APOGEE spectroscopic parameters are downloaded from the DR17.aspcapStar catalog on CASJobs, subject to the criteria `(a.aspcapflag & 261033871) = 0`, as well as `((a.teff_flag & 87903) = 0) AND (a.teff > -9999))`, and similarly for the parameters `logg`, `m_h`, and `fe_h`. We used the query described below.

```
SELECT a.apogee_id, b.gaiaedr3_source_id AS dr3_source_id,
CASE WHEN (((a.teff_flag & 87903)=0) AND (a.teff > -9999)) THEN a.teff ELSE null END AS teff,
CASE WHEN (((a.teff_flag & 87903)=0) AND (a.teff > -9999)) THEN a.teff_err ELSE null END AS teff_err,
CASE WHEN (((a.logg_flag & 87903)=0) AND (a.logg > -9999)) THEN a.logg ELSE null END AS logg,
CASE WHEN (((a.logg_flag & 87903)=0) AND (a.logg > -9999)) THEN a.logg_err ELSE null END AS
 logg_err,
CASE WHEN (((a.m_h_flag & 87903)=0) AND (a.m_h > -9999)) THEN a.m_h ELSE null END AS m_h,
CASE WHEN (((a.m_h_flag & 87903)=0) AND (a.m_h > -9999)) THEN a.m_h_err ELSE null END AS m_h_err,
CASE WHEN (((a.fe_h_flag & 87903)=0) AND (a.fe_h > -9999)) THEN fe_h ELSE null END AS fe_h,
CASE WHEN (((a.fe_h_flag & 87903)=0) AND (a.fe_h > -9999)) THEN fe_h_err ELSE null END AS fe_h_err into mydb.
  OutputFile from DR17.aspcapStar a
INNER JOIN DR17.apogeeStar b ON a.apstar_id=b.apstar_id
WHERE (a.aspcapflag & 261033871)=0
```

3. The main GALAH DR3 spectroscopic catalog, `GALAH_DR3_main_allstar_v2.fits`, is downloaded from the GALAH webpage at https://www.galah-survey.org/. We require that `snr_c3_iraf` > 30, `flag_sp` = 0, and `flag_fe_h` = 0.
4. The LAMOST DR7 data selection are as described by J. H. Hamer (2021).

ORCID iDs

David M. Nataf https://orcid.org/0000-0001-5825-4431
Kevin C. Schlaufman https://orcid.org/0000-0001-5761-6779
Henrique Reggiani https://orcid.org/0000-0001-6533-6179
Isabel Hahn https://orcid.org/0000-0003-4580-9893

References

Ahumada, R., Prieto, C. A., Almeida, A., et al. 2020, ApJS, 249, 3
Alves-Brito, A., Meléndez, J., Asplund, M., Ramírez, I., & Yong, D. 2010, A&A, 513, A35
An, D., Beers, T. C., & Chiti, A. 2024, ApJS, 272, 20
Astropy Collaboration, Robitaille, T. P., Tollerud, E. J., et al. 2013, A&A, 558, A33
Bailer-Jones, C. A. L., Rybizki, J., Fouesneau, M., Demleitner, M., & Andrae, R. 2021, AJ, 161, 147
Barnes, S. A. 2007, ApJ, 669, 1167
Bellazzini, M., Massari, D., Ceccarelli, E., et al. 2024, A&A, 683, A136
Bensby, T., Feltzing, S., & Oey, M. S. 2014, A&A, 562, A71
Bernstein, R., Shectman, S. A., Gunnels, S. M., Mochnacki, S., & Athey, A. E. 2003, Proc. SPIE, 4841, 1694
Bianchi, L., Shiao, B., & Thilker, D. 2017, ApJS, 230, 24
Bica, E., Ortolani, S., Barbuy, B., & Oliveira, R. A. P. 2024, A&A, 687, A201
Bland-Hawthorn, J., & Gerhard, O. 2016, ARA&A, 54, 529
Bovy, J. 2015, ApJS, 216, 29
Buchner, J., Georgakakis, A., Nandra, K., et al. 2014, A&A, 564, A125
Buder, S., Sharma, S., Kos, J., et al. 2021, MNRAS, 506, 150
Cantat-Gaudin, T., Anders, F., Castro-Ginard, A., et al. 2020, A&A, 640, A1
Capitanio, L., Lallement, R., Vergely, J. L., Elyajouri, M., & Monreal-Ibero, A. 2017, A&A, 606, A65
Carrasco, J. M., Weiler, M., Jordi, C., et al. 2021, A&A, 652, A86
Casagrande, L., Flynn, C., Portinari, L., Girardi, L., & Jimenez, R. 2007, MNRAS, 382, 1516
Casagrande, L., Schönrich, R., Asplund, M., et al. 2011, A&A, 530, A138
Casagrande, L., Silva Aguirre, V., Schlesinger, K. J., et al. 2016, MNRAS, 455, 987
Casagrande, L., & VandenBerg, D. A. 2014, MNRAS, 444, 392
Casamiquela, L., Blanco-Cuaresma, S., Carrera, R., et al. 2019, MNRAS, 490, 1821
Casey, A. R. 2014, PhD thesis, Australian National Univ., Canberra
Chanamé, J., & Ramírez, I. 2012, ApJ, 746, 102
Chance, Q., Foreman-Mackey, D., Ballard, S., et al. 2022, arXiv:2206.11275
Chen, X., Deng, L., de Grijs, R., et al. 2016, AJ, 152, 129
Choi, J., Dotter, A., Conroy, C., et al. 2016, ApJ, 823, 102
Christy, C. T., Jayasinghe, T., Stanek, K. Z., et al. 2023, MNRAS, 519, 5271
Cowan, J. J., Sneden, C., Burles, S., et al. 2002, ApJ, 572, 861
Cutri, R. M., Wright, E. L., Conrow, T., et al. 2021, yCat, 2328, 0
De Silva, G. M., Freeman, K. C., Bland-Hawthorn, J., et al. 2015, MNRAS, 449, 2604
Deng, L.-C., Newberg, H. J., Liu, C., et al. 2012, RAA, 12, 735
Donor, J., Frinchaboy, P. M., Cunha, K., et al. 2020, AJ, 159, 199
Dotter, A. 2016, ApJS, 222, 8
Drew, J. E., Gonzalez-Solares, E., Greimel, R., et al. 2014, MNRAS, 440, 2036
Feroz, F., & Hobson, M. P. 2008, MNRAS, 384, 449
Feroz, F., Hobson, M. P., & Bridges, M. 2009, MNRAS, 398, 1601
Feroz, F., Hobson, M. P., Cameron, E., & Pettitt, A. N. 2019, OJAp, 2, 10
Feuillet, D. K., Bovy, J., Holtzman, J., et al. 2018, MNRAS, 477, 2326
Flewelling, H. A., Magnier, E. A., Chambers, K. C., et al. 2020, ApJS, 251, 7
Gaia Collaboration, Babusiaux, C., van Leeuwen, F., et al. 2018a, A&A, 616, A10
Gaia Collaboration, Brown, A. G. A., Vallenari, A., et al. 2018b, A&A, 616, A1
Gaia Collaboration, Prusti, T., de Bruijne, J. H. J., et al. 2016, A&A, 595, A1
Gaia Collaboration, Smart, R. L., Sarro, L. M., et al. 2021, A&A, 649, A6
Gaia Collaboration, Vallenari, A., Brown, A. G. A., et al. 2023, A&A, 674, A1
Gennaro, M., Bik, A., Brandner, W., et al. 2012, A&A, 542, A74
Gennaro, M., Prada Moroni, P. G., & Degl'Innocenti, S. 2010, A&A, 518, A13
GRAVITY Collaboration, Abuter, R., Amorim, A., et al. 2018, A&A, 615, L15
Green, G. M., Schlafly, E., Zucker, C., Speagle, J. S., & Finkbeiner, D. 2019, ApJ, 887, 93
Hamer, J. H. 2021, RNAAS, 5, 24
Hayden, M. R., Bovy, J., Holtzman, J. A., et al. 2015, ApJ, 808, 132
Haywood, M. 2002, MNRAS, 337, 151
Haywood, M. 2008, MNRAS, 388, 1175
Heiter, U., Soubiran, C., Netopil, M., & Paunzen, E. 2014, A&A, 561, A93
Hendy, Y. H. M., & Abdel Rahman, H. I. 2022, JAsGe, 11, 166
Hong, J., Beers, T. C., Lee, Y. S., et al. 2024, ApJS, 273, 12
Horta, D., Mackereth, J. T., Schiavon, R. P., et al. 2021, MNRAS, 500, 5462
Huber, D., Bryson, S. T., Haas, M. R., et al. 2016, ApJS, 224, 2
Hunter, J. D. 2007, CSE, 9, 90
Ivezić, Ž., Kahn, S. M., Tyson, J. A., et al. 2019, ApJ, 873, 111
Jayasinghe, T., Kochanek, C. S., Stanek, K. Z., et al. 2021, MNRAS, 503, 200
Johnson, C. I., Rich, R. M., Young, M. D., et al. 2020, MNRAS, 499, 2357
Johnson, H. L., & Morgan, W. W. 1953, ApJ, 117, 313
Jones, E., Olyphant, T., & Peterson, P. 2001, SciPy: Open Source Scientific Tools for Python, http://www.scipy.org/
Jørgensen, B. R., & Lindegren, L. 2005, A&A, 436, 127
Jurić, M., Ivezić, Ž., Brooks, A., et al. 2008, ApJ, 673, 864
Katz, D., Sartoretti, P., Cropper, M., et al. 2019, A&A, 622, A205
Kelson, D. D. 2003, PASP, 115, 688
Kelson, D. D., Illingworth, G. D., van Dokkum, P. G., & Franx, M. 2000, ApJ, 531, 159
Kelson, D. D., Williams, R. J., Dressler, A., et al. 2014, ApJ, 783, 110
Kharchenko, N. V., Piskunov, A. E., Röser, S., Schilbach, E., & Scholz, R. D. 2005, A&A, 438, 1163

Kharchenko, N. V., Piskunov, A. E., Schilbach, E., Röser, S., & Scholz, R. D. 2013, A&A, 558, A53
Kilic, M., Munn, J. A., Harris, H. C., et al. 2017, ApJ, 837, 162
Kippenhahn, R., Weigert, A., & Weiss, A. 2013, Stellar Structure and Evolution (Berlin: Springer)
Kulkarni, S. R., Harrison, F. A., Grefenstette, B. W., et al. 2021, arXiv:2111.15608
Lallement, R., Vergely, J. L., Babusiaux, C., & Cox, N. L. J. 2022, A&A, 661, A147
Laureijs, R., Amiaux, J., Arduini, S., et al. 2011, arXiv:1110.3193
Li, T., Bedding, T. R., Christensen-Dalsgaard, J., et al. 2020, MNRAS, 495, 3431
Lindegren, L., Bastian, U., Biermann, M., et al. 2021, A&A, 649, A4
Liu, F., Asplund, M., Yong, D., et al. 2019, A&A, 627, A117
Lu, X., Yuan, H., Xu, S., et al. 2024, ApJS, 272, 49
Mackereth, J. T., & Bovy, J. 2018, PASP, 130, 114501
Mainzer, A., Grav, T., Bauer, J., et al. 2011, ApJ, 743, 156
Majewski, S. R., Schiavon, R. P., Frinchaboy, P. M., et al. 2017, AJ, 154, 94
Marín-Franch, A., Cassisi, S., Aparicio, A., & Pietrinferni, A. 2010, ApJ, 714, 1072
Masseron, T., & Gilmore, G. 2015, MNRAS, 453, 1855
McKinney, W. 2010, in Proc. 9th Python in Science Conf., ed. S. van der Walt & J. Millman, 56
McWilliam, A., & Rich, R. M. 1994, ApJS, 91, 749
Meibom, S., Grundahl, F., Clausen, J. V., et al. 2009, AJ, 137, 5086
Mendes de Oliveira, C., Ribeiro, T., Schoenell, W., et al. 2019, MNRAS, 489, 241
Miglio, A., Chiappini, C., Mackereth, J. T., et al. 2021, A&A, 645, A85
Mills, S. M., Fabrycky, D. C., Migaszewski, C., et al. 2016, Natur, 533, 509
Miyamoto, M., & Nagai, R. 1975, PASJ, 27, 533
Mohammed, S., Schiminovich, D., Hawkins, K., et al. 2019, ApJ, 872, 95
Montet, B. T., Morton, T. D., Foreman-Mackey, D., et al. 2015, ApJ, 809, 25
Morrissey, P., Conrow, T., Barlow, T. A., et al. 2007, ApJS, 173, 682
Morton, T. D. 2015, Isochrones: Stellar Model Grid Package, Astrophysics Source Code Library, ascl:1503.010
Nataf, D. M. 2015, MNRAS, 449, 1171
Nataf, D. M., Cassisi, S., Casagrande, L., Yuan, W., & Riess, A. G. 2021, ApJ, 910, 121
Nataf, D. M., Gould, A., & Pinsonneault, M. H. 2012, AcA, 62, 33
Navarro, J. F., Frenk, C. S., & White, S. D. M. 1996, ApJ, 462, 563
Oliphant, T. 2006, NumPy: A Guide to NumPy (USA: Trelgol Publishing), http://www.numpy.org/
Onken, C. A., Wolf, C., Bessell, M. S., et al. 2019, PASA, 36, e033
Pandey, A. K., Sandhu, T. S., Sagar, R., & Battinelli, P. 2010, MNRAS, 403, 1491
Paxton, B., Bildsten, L., Dotter, A., et al. 2011, ApJS, 192, 3
Paxton, B., Cantiello, M., Arras, P., et al. 2013, ApJS, 208, 4
Paxton, B., Marchant, P., Schwab, J., et al. 2015, ApJS, 220, 15
Poleski, R., Udalski, A., Bond, I. A., et al. 2017, A&A, 604, A103
Pont, F., & Eyer, L. 2004, MNRAS, 351, 487
Price-Whelan, A. M., Sipőcz, B. M., Günther, H. M., et al. 2018, AJ, 156, 123
Reggiani, H., Galarza, J. Y., Schlaufman, K. C., et al. 2024, AJ, 167, 45
Reggiani, H., Ji, A. P., Schlaufman, K. C., et al. 2022a, AJ, 163, 252
Reggiani, H., Schlaufman, K. C., Casey, A. R., Simon, J. D., & Ji, A. P. 2021, AJ, 162, 229
Reggiani, H., Schlaufman, K. C., & Casey, A. R. 2023, AJ, 166, 128
Reggiani, H., Schlaufman, K. C., Healy, B. F., Lothringer, J. D., & Sing, D. K. 2022b, AJ, 163, 159
Roussel, H., Gil de Paz, A., Seibert, M., et al. 2005, ApJ, 632, 227
Ruchti, G. R., Fulbright, J. P., Wyse, R. F. G., et al. 2011, ApJ, 737, 9
Salaris, M., & Cassisi, S. 2005, Evolution of Stars and Stellar Populations (New York: Wiley)
Sandquist, E. L., Latham, D. W., Mathieu, R. D., et al. 2021, AJ, 161, 59
Sarajedini, A., von Hippel, T., Kozhurina-Platais, V., & Demarque, P. 1999, AJ, 118, 2894
Schlafly, E. F., & Finkbeiner, D. P. 2011, ApJ, 737, 103
Schlafly, E. F., Green, G. M., Lang, D., et al. 2018, ApJS, 234, 39
Schlaufman, K. C., Thompson, I. B., & Casey, A. R. 2018, ApJ, 867, 98
Schlegel, D. J., Finkbeiner, D. P., & Davis, M. 1998, ApJ, 500, 525
Schonrich, R. 2012, MNRAS, 427, 274
Schönrich, R., & Bergemann, M. 2014, MNRAS, 443, 698
Schönrich, R., & Binney, J. 2009, MNRAS, 399, 1145
Schönrich, R., Binney, J., & Dehnen, W. 2010, MNRAS, 403, 1829
Schönrich, R., McMillan, P., & Eyer, L. 2019, MNRAS, 487, 3568
Shappee, B. J., Prieto, J. L., Grupe, D., et al. 2014, ApJ, 788, 48
Sharma, S., Stello, D., Bland-Hawthorn, J., et al. 2019, MNRAS, 490, 5335
Shectman, S. A., & Johns, M. 2003, Proc. SPIE, 4837, 910
Shvartzvald, Y., Waxman, E., Gal-Yam, A., et al. 2024, ApJ, 964, 74
Sichevskij, S. G., Mironov, A. V., & Malkov, O. Y. 2014, AstBu, 69, 160
Siegel, M. H., Hoversten, E. A., Roming, P. W. A., et al. 2010, ApJ, 725, 1215
Skrutskie, M. F., Cutri, R. M., Stiening, R., et al. 2006, AJ, 131, 1163
Sneden, C., Kraft, R. P., Prosser, C. F., & Langer, G. E. 1991, AJ, 102, 2001
Sneden, C., McWilliam, A., Preston, G. W., et al. 1996, ApJ, 467, 819
Soderblom, D. R. 2010, ARA&A, 48, 581
Spergel, D., Gehrels, N., Baltay, C., et al. 2015, arXiv:1503.03757
Spina, L., Ting, Y. S., De Silva, G. M., et al. 2021, MNRAS, 503, 3279
Stello, D., Vanderburg, A., Casagrande, L., et al. 2016, ApJ, 832, 133
Strömgren, B. 1966, ARA&A, 4, 433
Taylor, B. J. 2007, AJ, 133, 370
Taylor, M. B. 2005, in ASP Conf. Ser. 347, Astronomical Data Analysis Software and Systems XIV, ed. P. Shopbell & M. Britton (San Francisco, CA: ASP), 29
Tonry, J. L., Stubbs, C. W., Lykke, K. R., et al. 2012, ApJ, 750, 99
Twarog, B. A. 1980, ApJ, 242, 242
Valcarce, A. A. R., Catelan, M., & Sweigart, A. V. 2012, A&A, 547, A5
Valle, G., Dell'Omodarme, M., Prada Moroni, P. G., & Degl'Innocenti, S. 2015, A&A, 577, A72
VandenBerg, D. A., Gustafsson, B., Edvardsson, B., Eriksson, K., & Ferguson, J. 2007, ApJL, 666, L105
Vergely, J. L., Lallement, R., & Cox, N. L. J. 2022, A&A, 664, A174
Viani, L., & Basu, S. 2017, EPJWC, 160, 05005
Virtanen, P., Gommers, R., Oliphant, T. E., et al. 2020, NatMe, 17, 261
Witten, C. E. C., Aguado, D. S., Sanders, J. L., et al. 2022, MNRAS, 516, 3254
Wright, E. L., Eisenhardt, P. R. M., Mainzer, A. K., et al. 2010, AJ, 140, 1868
Xiang, M., & Rix, H.-W. 2022, Natur, 603, 599
Xiang, M., Ting, Y.-S., Rix, H.-W., et al. 2019, ApJS, 245, 34
Xiang, M. S., Liu, X. W., Yuan, H. B., et al. 2015, MNRAS, 448, 822
Zhang, H., Ardern-Arentsen, A., & Belokurov, V. 2024, MNRAS, 533, 889
Zhao, G., Zhao, Y.-H., Chu, Y.-Q., Jing, Y.-P., & Deng, L.-C. 2012, RAA, 12, 723